CRANFIELD UNIVERSITY

ATHANASIA NIANIOURA-KARAMOUSALIDOU

WHEEL RIM TYRE CFD MODELLING

SCHOOL OF AEROSPACE, TRANSPORT AND MANUFACTURING
Computational Fluid Dynamics

MSc
Academic Year: 2016–2017

Supervisor: Dr Antonios F. Antoniadis
August 2017

CRANFIELD UNIVERSITY

SCHOOL OF AEROSPACE, TRANSPORT AND MANUFACTURING
Computational Fluid Dynamics

MSc

Academic Year: 2016–2017

ATHANASIA NIANIOURA-KARAMOUSALIDOU

WHEEL RIM TYRE CFD MODELLING

Supervisor: Dr Antonios F. Antoniadis
August 2017

This thesis is submitted in partial fulfilment of the requirements for the degree of MSc.

© Cranfield University 2017. All rights reserved. No part of this publication may be reproduced without the written permission of the copyright owner.

Abstract

In this thesis, the flow around an isolated wheel at $Re = 5.3 \cdot 10^5$ is investigated for different rotation modelling techniques and geometrical characteristics. Both the steady and unsteady density-based RANS solver is used with the *Realizable* k-ε model.

Regarding the rotation of the wheel, three methods are utilised. Initially, simple rotating boundary conditions are applied, and then, the sliding mesh method is used. The application of the overset mesh method is also attempted, but on a slightly modified geometry that does not correspond exactly to the baseline case. All cases are compared to experimental results for several aspects of the flow and a Grid Convergence Study is performed for the steady state simulation in order to validate the results.

Subsequently, more geometries are investigated. Grooves and realistic rims are added to the baseline geometry separately and combined in order to create three more cases. The alterations in the flow around them are studied by examining the forces coefficients, the vortical structures and the pressure field around the wheels. A comparison is also made regarding the computational cost for the rotation modelling methods and the forces distribution on different regions of the wheel.

The appropriate height of the step used in the contact patch region is studied since it can affect the accuracy of every model significantly. Interesting results were produced, especially concerning the smallest step heights. The drag coefficient was affected greatly, but the lift was not influenced accordingly.

Finally, three camber angles, -1^o, -2^o and -3^o are applied to the grooved tyre model. The flow field and specifically the wake is altered significantly, due to tilt of the vertical axis. However, there are no previous studies to compare the resulting structures that occur on the top of the wheel.

Keywords

isolated tyre; CFD; Fluent; rotating; sliding; overset; contact patch; camber angle.

Contents

Abstract v

Table of Contents vii

List of Figures ix

List of Tables xi

List of Abbreviations xiii

Acknowledgements xv

1 Introduction 1
- 1.1 Overview of wheel aerodynamics . . . 2
- 1.2 Literature Review . . . 5
- 1.3 Objectives . . . 17
- 1.4 Structure of the thesis . . . 17

2 Theoretical Background and Methodology 19
- 2.1 Governing Equations . . . 19
- 2.2 Rotation Modelling . . . 22
- 2.3 Overset Mesh . . . 27
- 2.4 Geometries . . . 28
- 2.5 Grid Generation Strategy . . . 34
- 2.6 Overset model and mesh . . . 37
- 2.7 Solver Setup . . . 39

3 Preliminary Study 43
- 3.1 Grid Convergence Study . . . 43
- 3.2 Clustered Grid . . . 46
- 3.3 Pressure Distribution . . . 47
- 3.4 Error Calculation . . . 49
- 3.5 Sliding Mesh . . . 49

3.6 Overset Mesh 51
3.7 Flow Field 52

4 Results and Discussion **55**
4.1 Comparison of Different Models 55
4.2 Step Height Sensitivity Study 67
4.3 Camber Angle Sensitivity Study 71

5 Conclusions and Future Work **75**

A Meshes **79**

B C_L and C_D over time for unsteady simulations **81**

C Matlab Codes **83**
C.1 C_P transformation from Cartesian to Polar coordinates 83
C.2 Error Norms calculation 85

References **87**

List of Figures

1.1 Main vortices produced by a wheel [1] . . . 3
1.2 General isolated wheel flow [2] . . . 4

2.1 MRF [3] . . . 24
2.2 Sliding mesh method [3] . . . 25
2.3 Overset mesh method [3] . . . 27
2.5 Tyre geometries . . . 31
2.6 Camber angles . . . 32
2.7 Effect of different step heights on wheel geometry . . . 33
2.8 Computational Domain . . . 35
2.9 Transition from prismatic to tetrahedral elements . . . 36
2.10 Contact patch . . . 36
2.11 Sliding mesh geometry . . . 37
2.12 Initial concept of overset topology . . . 38
2.13 Overset mesh . . . 39
2.14 Boundary Conditions . . . 40

3.1 Refinement area . . . 46
3.2 . . . 47
3.3 Pressure coefficient on different lines along the wheel's circumference . . . 48
3.4 C_D and C_L over time . . . 50
3.5 Total pressure along the central plane . . . 52
3.6 Pressure contours and streamlines on the centreline . . . 54
3.7 Qcriterion . . . 54

4.1 Pressure distribution on the centreline of the wheel for all cases . . . 59
4.2 C_P contours and streamlines on the centreline . . . 60
4.3 Qcriterion isosurfaces for the three wheel models . . . 62
4.4 Computational cost of the baseline case . . . 63
4.5 Computational cost of the grooved wheel . . . 64
4.6 Division of the wheel into regions . . . 65
4.7 Drag and Lift coefficients for the step heights . . . 67
4.8 C_P contours and streamlines on the ground plane . . . 69

4.9 Isosurfaces of Q criterion for different camber angles 73

A.1 Baseline clustered box 79
A.2 Frontal view - grooved wheel 79
A.3 Detailed view - grooved wheel 80
A.4 Side view - wheel with rim 80
A.5 Detailed view - wheel with rim 80

B.1 C_L and C_D over time for the grooved wheel 81
B.2 C_L and C_D over time for the wheel with a rim 82
B.3 C_L and C_D over time for the grooved wheel with a rim 82

List of Tables

1.1 Turbulence Models in literature 16

2.1 Geometrical characteristics 28
2.2 Flow characteristics 29
2.3 Step heights 33
2.4 Boundary Conditions 40

3.1 Three grid levels 44
3.2 Lift and Drag Coefficient using different mesh levels 45
3.3 Grid converge index analysis 46
3.4 C_P Errors 49
3.5 C_D and C_L and relative errors 50
3.6 C_D and C_L for the overset mesh 51

4.1 C_D and C_L for all models 56
4.2 Grooved wheel grid levels 57
4.3 C_D and C_L for different mesh levels 57
4.4 Grid converge index analysis 57
4.5 Drag distribution on the wheel 66
4.6 Lift distribution on the wheel 66
4.7 C_D and C_L for all camber angles 71

List of Abbreviations

CAD	Computer Aided Design
CFD	Computational Fluid Dynamics
DES	Detached Eddy Simulation
FEA	Finite Element Analysis
GCI	Grid Convergence Index
IDDES	Improved Delayed Detached Eddy Simulation
LBM	Lattice Boltzmann Method
LDA	Laser Doppler Anemometry
LES	Large Eddy Simulation
MRF	Multiple Reference Frame
RANS	Reynolds Averaged Navier-Stokes
RBC	Rotating Boundary Condition
SATM	School of Aerospace, Technology and Manufacturing
URANS	Unsteady Reynolds Averaged Navier-Stokes

Nomenclature

γ	Observed order of truncation rate $[-]$
ε	Turbulent dissipation rate $[m^2/s^3]$

ε_{12}	Relative differences between fine and medium mesh solution $[-]$
ε_{23}	Relative differences between fine and medium mesh solution $[-]$
μ	Dynamic viscosity $[Pa \cdot s]$
ν	Kinematic viscosity $[m^2/s^2]$
ρ	Density $[kg/m^3]$
$\bar{\bar{\tau}}$	Stress Tensor
ω	Rotational Velocity $[m/s]$
A	Surface $[m^2]$
C_D	Drag coefficient $[-]$
C_L	Lift coefficient $[-]$
C_P	Pressure coefficient $[-]$
k	Turbulent kinetic energy $[m^2/s^2]$
Ma	Mach number $[-]$
p	Pressure field $[Pa]$
Re	Reynolds number $[-]$
r	Refinement ratio $[-]$
t, T	Time $[s]$
$\vec{u}, \vec{v}, \vec{w}$	Components of velocity vector in vector notation $[m/s]$
u_i, v_i, w_i	Velocity vector in index notation $[m]$
V	Volume $[m^3]$

Acknowledgements

I would like to thank my supervisor Dr. Antonis F. Antoniadis for his encouragement and guidance in the course of this thesis and my colleague Carolina Olmedo Egea for our constant cooperation through this whole project.

I am sincerely thankful to my flatmates and friends, Olivia, Anna, Murad, Gabri, Aleix, Julen, Stelina, Ramon, Pablo, for making this entire year a great adventure. I hope in the future we get to spend even more time together, with less studying and even more fun.

I would also like to thank Dimitris for surviving after a year of constant nagging from my part and not complaining about having to hear everything about this project.

Finally, I am grateful to my parents for supporting my choices all these years and always being there for me no matter what.

Chapter 1

Introduction

This project investigates the aerodynamics of exposed isolated car wheels. Both steady state and transient simulations were performed for different geometries to compare the change in aerodynamic characteristics. A baseline simple geometry was initially studied, while some more complex features are added later. The majority of the work focuses on either steady state or time-averaged data, although some unsteady flow features are exhibited for all the cases. A key element to this project is the comparison between different techniques for modelling rotation since they can significantly affect the results. Furthermore, some aspects of the geometries that are crucial for the overall aerodynamic behaviour are investigated.

This chapter gives a brief introduction into wheel aerodynamics and how they affect vehicle aerodynamics. The research that was conducted for this project is presented in order to provide the context of this investigation and give some insight into the contents of this thesis. Finally, the objectives are highlighted and the thesis structure is specified.

1.1 Overview of wheel aerodynamics

There has been growing emphasis on fuel economy through improving aerodynamic performance. In moderate cruising speeds, the vehicle power requirements due to aerodynamic resistance can be greater than the power needed to overcome rolling resistance of the tyres. Since the greatest source of aerodynamic resistance is the flow over the exterior of the vehicle, it has become increasingly important to reduce it. Therefore, the most significant aerodynamic characteristic of a vehicle is the drag force, which represents the total aerodynamic force resisting forward motion and can be expressed as:

$$Drag = \frac{1}{2}\rho V^2 A C_D \tag{1.1}$$

where ρ is the density of the air, V is the vehicle's speed and A is the frontal area. The factor C_D, the drag coefficient, depends strongly on the shape of the body or vehicle and provides a good indicator of its overall aerodynamic resistance.

Another important aspect of the behaviour of a road vehicle is its aerodynamic lift. It can affect the drag indirectly, but more significantly, it is vital for achieving stability and improving roadholding, particularly in the case of racing cars. Lift can be created by the differences in pressure between upper and lower surfaces, and thus, is strongly dependent on the flow on the underbody of the vehicle. The generation of negative lift, or downforce, has been a major preoccupation of the aerodynamic design process [4]. The expression for aerodynamic lift is formulated accordingly to the one for drag and is:

$$Lift = \frac{1}{2}\rho V^2 A C_L \tag{1.2}$$

For the purpose of this project both forces will be calculated through simulations and

thus, the two coefficient will be derived as:

$$C_D = \frac{2D}{\rho V^2 A} \tag{1.3}$$

$$C_L = \frac{2L}{\rho V^2 A} \tag{1.4}$$

Wheels are one of the most influential components affecting vehicle aerodynamics. The flow around an isolated wheel can be compared to the that around a cylinder. There is a slight periodic wake shedding, affecting a large region of separated flow behind the wheel. The wake is highly turbulent and strong trailing vortices tend to appear producing high aerodynamic drag. Due to the contact to the ground, lift also is created on the wheel, which can be a significant issue for vehicle aerodynamics. At the front of a wheel, there is a large high pressure area around the stagnation point, causing a small flow recirculation region at the bottom half [5], [6]. The flow at the sides can be equally important since

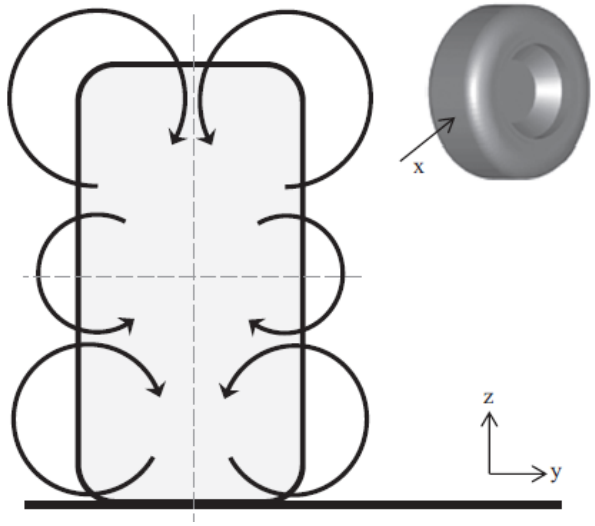

Figure 1.1: Main vortices produced by a wheel [1]

strong vortices tend to be created there. Counter-rotating vortices are created both at the top and the bottom of the wheel, while, depending on the Reynolds number, another pair

might occur at the middle part. These trail downstream causing even higher drag and creating the big wake region. The horseshoe vortex that also appears in that area tends to reinforce those longitudinal vortices. There is also a significant differentiation between the aerodynamic behaviour of a stationary and a rotating wheel. For a stationary wheel, the separation point is located very close to the highest point. However, on a rotating wheel, the top point is moving in opposite direction to the air stream, causing the flow to separate earlier, usually in the front top quarter of the wheel [7]. This also creates an arch shaped vortex at the top of the wheel, which can be seen in Figure 1.2. Furthermore, the vortices created behind the stationary wheel are weaker than those behind the rotating. The separated region formed on the ground and in the near wake of the wheel is also smaller in the rotating case.

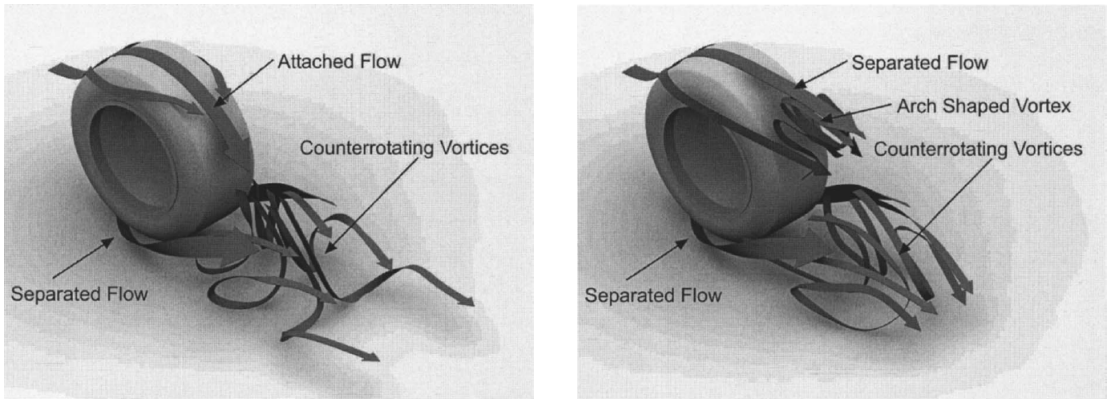

(a) Stationary wheel (b) Rotating wheel

Figure 1.2: General isolated wheel flow [2]

1.2 Literature Review

The objectives of this chapter are to critically review the previous research and current level of understanding of wheel aerodynamics. While literature concerning experimental case studies is discussed, the main focus is put on the computational point of view. The modelling of wheels is thoroughly analysed, in different scenarios. Specifically, literature related to the effects of wheel modelling in vehicle aerodynamics is examined, while emphasis is given on the differences between isolated and shrouded wheels, in order to assist in the understanding of the modelling approaches most appropriate for each case. Finally, the effects of the tyre's geometry are reviewed, since the incorporation of more detailed aspects is much more realistic in terms of flow physics. A comparison between the results of different turbulence models is also presented.

1.2.1 Effect of Wheels in Vehicle Aerodynamics

The aerodynamic influence of wheels has proved to be significant in the behaviour of vehicle and thus, has been studied extensively both experimentally and numerically.
A comparison between LDV measurements and CFD simulations has been investigated by Wäschle [8]. The main aim was to examine the effects of the wheels' rotation and the differences caused by rim geometries. The experiment was conducted for both a simplified quarter scale vehicle model and a fully detailed production car. In order to simulate the rotation of the wheels, the Multiple Reference Frame method was used, while three different rim types were evaluated. It was shown, that the rotation of the wheel caused local drag and lift reduction at the front wheels, as well as less flow separation at the contact patches. Furthermore, when stationary wheels were used, wide wakes occurred behind them, causing an obstruction to the flow expansion by the rear diffuser. This effect could disappear with the use of rotating wheels, and shows the importance of their incor-

poration in the aerodynamic design of a vehicle.

A small hatchback vehicle was used by Lounsberry et al. [9] to compare the outcomes of a wind tunnel experiment and CFD simulations. Both were static tests and no rotation was applied to the wheels, but the detailed geometry of the whole car, including the wheels, whose CAD geometry was a result of 3D scanning, was of great importance to the researchers. The results showed great agreement in general. This was attributed to a number of reasons, among which the floor boundary layer, the detailed geometry of the model and the appropriate resolution of the grid in these detailed regions, were highlighted as to be of great importance.

The aerodynamic performance of different configurations of a car was tested by Kandasamy et al. [10] in both experiments and CFD simulations. The different approaches of modelling rotating wheels were compared since simulations were performed using the rotating wall boundary condition for the wheels and tires and the MRF method was applied to the flow region around the spokes. The sliding mesh method was also applied to the non-axisymmetric part of the rims to have a more realistic representation of the rotating wheel, while the tyre treads were represented by a rotating wall boundary condition. The MRF and rotating wall methods showed a maximum error in drag of 5% compared to 2% produced by the sliding mesh method. Generally, the sliding mesh method produced much more accurate and consistent results, even for different configurations of the car, but it comes with a significantly higher computational cost.

Koitrand and Rehnberg [11] also investigated the effects of using a rotating wall boundary and a moving wall to model the wheels. Only the spokes were enclosed in the MRF regions, while the rest of the wheels and tyres were modelled as rotating walls. Several different combinations between stationary and moving ground and rotating either front of rear wheels were compared on two car models. They provided a thorough discussion on the effects of different boundary conditions on the aerodynamic behaviour of the vehicles. The results showed good agreement with previous experiments and simulations, as well as great consistency between the two cars. The rotation of the wheels in any combination causes the flow field to change significantly, while the moving floor has also important effects. Finally, the transient solver which was used can offer the possibility to have a better understanding in the wake region. The researchers conclude that it would be beneficial during the design of a vehicle to initially use stationary simulations, since they provide reasonable results.

The most recent study regarding full body aerodynamics has been conducted by Simmonds et al. [12] with the purpose of identifying the cooling drag of three vehicles. In order to increase the accuracy of their simulations, the wheels were modelled using the MRF method in combination with RANS and the sliding mesh approach for the IDDES and LBM methodologies. For the RANS simulations, all the turbulence models showed similar behaviour, but their accuracy is questionable. On the other hand, both transient methods provided trustworthy results, when compared to previous experimental data.

1.2.2 Wheels in Wheelhouse Cavities

Since in most cases simulating a complete vehicle can be significantly expensive computationally, a compromise that is usually made by researchers is the simulation of the

system of a wheel in a wheelhouse cavity. This can provide a satisfying base to make conclusions on the effect that different wheel configurations will have on a car.

Axon, Garry and Howell [13] were the first to provide both experimental and computational data on a shrouded wheel. The experimental model included a moving groundplane, while pressure measurements were also taken in the wheelhouse cavity. A steady state simulation was performed on almost the same model for both a stationary and a rotating wheel. The results concluded that the rotating wheel on a moving ground produced more drag, while good agreement was shown on the flow phenomena qualitatively, but not quantitatively.

Further experimental measurements and CFD simulations on a wheel in a wheelhouse cavity by Skea, Bullen and Qiao [14]. Two wheel models were used for the experiment and the rotation was achieved by the moving floor of a wind tunnel, while measurements were taken for a stationary and a rotating wheel. The CFD simulation was designed in such a way, as to match the experimental conditions, with a rotating wheel and a moving ground, as well as a stationary system. The results showed that the main features of the flow were predicted by CFD. The main characteristics of the Cp profiles were predicted but many of the phenomena in the wheelhouse cavity could not be identified in the results.

Krajnovic, Sarmast and Basara [15] used a model created for a previous experiment to perform large eddy simulations on a shrouded wheel in order to determine the impact that the width of the wheel housing has on the flow. The instantaneous flow fields showed that between the wheel and the wheelhouse cavity, the flow structures are extremely complex and strongly depend on the width of the housing. When compared to the previous experimental data, which reported important uncertainties for drag and lift, the simulations

predicted different pressure distribution in the wheelhouse. The researchers concluded that the difference in width of the housing did not affect significantly the flow structure. As a continuation of the previous work, Krajnovic [16] assesses the simulations that were performed and a suggests which information is appropriate to be extracted by an LES simulation on automotive applications. After reevaluating the previous data, he concludes that their importance lies in the instantaneous flow structures, which can provide further understanding of the complexity of the flow in the wheelhouse.

1.2.3 Isolated Wheels

A step further from studying shrouded wheels, is research on the aerodynamic behaviour of isolated wheels. This can have more applications rather than purely automotive, since it is also a field of interest in the aerospace sector. The simpler general geometry and flow structure gives more way for further unsteady and more detailed cases to be studied, both experimentally, and computationally. Therefore, isolated wheels have been a popular research topic in recent years.

Probably the most important early work concerning the aerodynamic behaviour of isolated wheels is that of Fackrell [17]. Until today, it has been the main base of comparison for computational results, while several researchers have performed similar experiments to compare data. The experiments were performed on six different wheel configurations, which included three different tread widths and two edge profiles. The wheels rotated freely and were in contact with a moving floor, reassuring that there was no slipping between the two surfaces. The results showed that both drag and lift coefficients increase with the width, but when the width of the tread was taken into account during the calculation, the drag coefficient was almost constant. The pressure distribution was also

discussed for different parts of the wheel, and it was found that the edge shape had little effect at the centre line regardless of the width of the wheel. Other than that, the specific distribution was case specific, and differences existed depending on the features. Subsequently, rotation had interesting effects, since when it was applied, both drag and lift were reduced. Thus, it was concluded that the early separation of the flow over the top of the wheel was caused by the rotation and was not a characteristic of the wheel. The results were also not very sensitive to wind speed variations. Generally, these results have been compared with several experimental and computational data since then.

Based on this experiment, Axon and Garry [18] performed CFD simulations on a stationary and a rotating isolated wheel to test the accuracy of CFD. The wheel's rotation was modeled by a rotating wall boundary condition on the wheel and a moving wall condition on the groundplane, while the contact patch was cut horizontally for a radius of 10 degrees. The results showed all the flow structures that were present in the experimental work in both the stationary and the rotating wheel and confirmed the effect of reduced lift and drag that occur in the case of the rotating wheel.

An experimental and CFD analysis were performed on a wheel model by Wäscle et al. [19] in order to compare two different CFD codes, STAR-CD and EXA PowerFLOW. LDA measurements were taken around a rotating wheel on a moving belt, while this was modeled with the use of the MRF method for the rims and a moving wall condition was set for the ground. The comparison in the end showed that both codes produced trustworthy results, but the steady-state method was preferred, since it show greater accuracy in some areas around the wheel.

The same modeling strategy for a full sized wheel was applied by McManus and Zhang

[2], along with rotating boundary conditions on the wheel and moving groundplane. Unsteady simulations were performed in order to determine the grid dependence and a detailed flow field. The study revealed new flow structures, while showed great agreement with Fackrell's experimental data generally, on both surface pressures and forces. It also showed to have very small grid dependency.

More similar studies have investigated the flow around a stationary and rotating wheel, coming up with either computational [20, 21, 22, 23] or experimental [24] results. The experimental study focused on producing data, through PIV measurements, in order to have a base of comparison for further computational studies. It also included deformation data which can be used for more accurate wheel modeling. Regarding the computational studies, the rotating wall boundary condition and the MRF method were used, since the sliding mesh is considered too costly. The rotating wheel case is handled both as steady [21, 22] and an unsteady problem, while, also LES simulations were performed either on a full sized [20] or a modeled wheel [23]. The results were generally accurate compared to experimental studies, but the LES simulations revealed new flow structures, that can not be seen in steady-state simulations. The wake regions have also been more thoroughly studied in the transient cases, giving some new insight on the flow structure that occur there, and in general wheel aerodynamics.

The most recent research concerned with wheel aerodynamics is an experimental study by Spagnolo et al. [25] which apart from a single isolated wheel, also deals with the aerodynamics of tandem wheels in contact with a stationary or moving ground, representing a simplified landing landing gear. Particle Image Velocimetry was used in order to capture the flow characteristics, while special care was taken during the measurement process in order to be able to recognise detailed flow structures in both wheels. The measurements

showed low sensitivity to Reynolds number and a limited effect of the distance between the axes on the drag of the whole system.

1.2.4 Effects of Wheel Geometry

Wheels have a large influence on overall vehicle aerodynamics, since they strongly interact with several other parts that are crucial for the aerodynamic performance. This shows how important it is to use models that are as realistic as possible in simulations. Therefore, new studies try to incorporate as many features as possible, such as the spokes, treads and even the deformation of the wheel in order to perform correlation studies.

Since this detailed approach on tires is relatively recent, it is important to have reliable experimental data. Wittmeier et al. [26] measured different production tyres in full size, but also a quarter scale model of the same tyres. The full sized tyres were fully deformable, but the scaled ones were rigid. The researchers found out that even small differences in the geometry can cause significant differences in drag, which is mostly defined by the lower part of the wheel, and so, not affected by the wheelhouse. Subsequently, the shoulder of the tyre, had a major effect on the aerodynamic characteristics and should be looked into, when trying to optimise the efficiency of a vehicle.

Landström et al. [27] tested both experimentally and computationally different wheel configurations, where the spokes were covered in different degrees. The wind tunnel testing was conducted on a full scale car, but the experimental and computational models had minor differences. The results showed that, when the front wheels were closed, the computational model could not predict the flow structures correctly. The optimised configuration was to have the rear wheels closed, since in this case, a great reduction in drag

was noticed, while closing the front wheels caused more complex flow phenomena.

A really detailed study was performed by Hobeika, Sebben and Landstrom [28], who focused not only on the different rim types but also investigated the deformation and different kind of grooves on the tyre. The experiment was performed in a full scale car and a moving ground belt was installed. The configurations tested numerically included four different tyre pattern features and four different rim types.The contact patch was modeled differently, and the grooves were either interrupted or had less height according to the deformation that was applied.The MRF method was used in order to model the rotation of the wheels. It has been found, that the tyre's patterns cause differences in the flow characteristics, altering drag and lift, as did the rim configurations. The researchers suggest this type of deformation to be used in future simulations, since it is more realistic and commented that the use of a sliding mesh would be more appropriate for such sensitive flow.

Gleason et al. [29], also performed an experimental and computational study on different configurations of wheels, including grooved tyres. The geometry of the static wheel was a result of 3D printing, while the rotating model was a simplified version of the previous. The deformation of the tyre was also taken into account in the modelling of the contact patch. Again the importance of detailed tyre models is stressed by the researchers and they found that the simulations were able to accurately predict the drag and the differences of the flow structures. They also suggested finer mesh resolution in order to have more detailed results and analysis.

An experimental and CFD analysis were also performed on a production car tyre by Schnepf, Tesch and Indinger [30]. With both methods, they accounted for the forces

applied on the wheel and their realistic rotation, which both determined the deformation of the wheel. For the numerical model, the sliding mesh method was used to model the rotation and a moving wall boundary condition was applied to the groundplane. The simulations were considered to be reasonably accurate, and the suggestion made was to study the whole car and not just the isolated wheel, in order to have more immediately applicable results.

A different study that also used the sliding mesh method, by D'Hooge et al. [31], introduced different rim designs of a full size wheel, which were tested both experimentally and computationally, in order to calculate the power loss connected to the wheels. The results were qualitatively similar, since both led to the same optimised wheel configuration. However certain limitations are set when comparing so accurate testing and CFD results.

Schnepf, Schütz and Indinger [32] performed CFD simulations and experiments on a fully deformable treaded tyre. The deformations were a result of the applied forces and the rotation of the tyre, and the final geometry of the contact patch was defined by an FEA model. The numerical model was unable to capture all the flow structures that were seen in the experimental data. It has also been found, that the treaded tyre is much more sensitive to load variations, causing changes in the contact patch separation.

In order to investigate the flow around isolated wheels several simplifications are made, which are thought to have minimal effect on the flow. Diasinos, Barber and Doig [1] studied these simplifications, such as using a constant radius shoulder on the tyre, wheels without hubs on the rim area and altering the contact patch area and the step height. The limitations of modelling the contact patch area accurately has been stressed in this study, while the other simplifications were noted to mostly affect the lift, but the drag was shown

to be relatively stable.

Further simulations on a simple treaded wheel were performed by Gautam and Chandy [33], combining the previously discussed topics with the acoustics of the tyre. A simplified deformation of the grooves, created by a piston-like motion of the bottom wall. A simulation of the air being pumped in and out of the grooves was incorporated in order to produce accurate acoustic data. The results in this case study are not important in this case, since they are aimed towards a different direction. However, it is important to note that the same methodology used for this study, could be applied in a CFD model focused on aerodynamic optimisation.

The latest study concerning different tyre geometries has been performed by Lew et al. [34] and used a Lattice Boltzmann method based solver in combination with an immersed boundary method based approach. A fully treaded tyre was simulated and compared to previous experimental results, while the changes that occur in the wake when using a loaded tyre were discussed. A jetting effect was noticed in the tread area when it was in contact with the ground. Overall, the treaded tyre produced much more realistic results than a simple grooved tyre. The researchers also concluded that the computed floor wake structure differs from that of a real loaded tyre because of the absence of the bulge in the contact patch, but the results can be imitated by having the treads penetrate the ground plane in different heights.

1.2.5 Turbulence Models

For the simulations that were described above several turbulence models were used. Those studies that used either RANS or URANS are presented in Table 1.1 in more detail, as to the models that were applied.

Study	**Model**	**Solution Method**	**Turbulence Model**
Simmonds et al. [12]	Full-scale car	RANS	Realizable $\kappa-\varepsilon$ $\kappa-\omega$ SST Spalart-Allmaras
Axon [18]	Shrouded Wheel	RANS	RNG $\kappa-\varepsilon$ Standard $\kappa-\varepsilon$
Wäschle [8]	Full-scale car	RANS	Standard $\kappa-\varepsilon$
Skea & Bullen & Qia [14]	Shrouded Wheel	URANS	RNG $\kappa-\varepsilon$
Lesniewicz & Kulak & Karczewski [**?**]	Isolated Wheel	RANS	SST
McManus & Zhang [2]	Isolated Wheel	URANS	Realizable $\kappa-\varepsilon$ Spalart-Allmaras
Dassanayake [20]	Isolated Wheel	URANS	$\kappa-\omega$ SST
Axon & Garry & Howell [13]	Isolated Wheel	RANS	RNG $\kappa-\varepsilon$
Axerio et al. [23]	Isolated Wheel	URANS	$\kappa-\omega$ SST
Landström et al. [27]	Full-scale car	RANS	Realizable $\kappa-\varepsilon$
Hobeika & Sebben & Landstrom [28]	Isolated Wheel	RANS	Realizable $\kappa-\varepsilon$

Table 1.1: Turbulence Models in literature

1.3 Objectives

The present project aims at identifying the flow features around an isolated wheel rim tyre system with different configurations. A baseline simple case is compared to three different configurations, one with a grooved tyre, one with a realistic rim and the final with the combination of both geometrical characteristics. All cases are simulated in both steady state, with rotating boundary condition at the wheel surface and with the overset mesh method, and transient utilising the sliding mesh technique. These simulations are performed in order to compare the accuracy and computational cost of the methods, as well as to identify different flow features of each case and to isolate which geometrical characteristic causes the phenomena.

1.4 Structure of the thesis

The main part of this thesis will involve the statement of the basic theoretical background concerning the most significant governing equations as well as the theory behind the methods that will be used and the solver setup for all the cases. The results will be presented in the separately for the baseline model, in order to have a core of data for comparison. The flow field will be examined by contrasting the overall drag coefficients, the pressure coefficient in specific locations, the main phenomena that occur around the wheel and their computational cost. These will be presented and discussed initially for the baseline case, and then for the three different wheel configurations in separate chapters. Finally, the conclusions of all outcomes are going to be drawn and future work that should be done will be discussed.

Chapter 2

Theoretical Background and Methodology

2.1 Governing Equations

2.1.1 Mass and Momentum Conservation Equations

The solver used for the present study is ANSYS Fluent, which solves the conservation equations for momentum and mass. Additional transport equations are solved for turbulent flows. For this project, since it will be: $Ma \leq 0.2$, the density will be considered constant throughout the simulations, thus ending up with the simplified continuity equation as shown in equation 2.1 [3].

$$\frac{\partial \rho}{\partial t} + \bigtriangledown \cdot (\rho \vec{v}) = 0 \tag{2.1}$$

This is the general form of the mass conservation equation, where ρ is the density of the fluid, t the variable time and $\vec{v}$ the velocity vector. Then, the conservation of momentum can be expressed as:

$$\frac{\partial}{\partial t}(\rho\vec{v}) + \bigtriangledown\cdot(\rho\vec{v}\vec{v}) = -\bigtriangledown p + \bigtriangledown\cdot(\bar{\bar{\tau}}) + \rho\vec{g} + \vec{F} \tag{2.2}$$

where p is the static pressure. The gravitational body forces, $\rho\vec{g}$ as well as external body forces will not be taken into account and the stress tensor is given by:

$$\bar{\bar{\tau}} = \mu\left[\left(\bigtriangledown\vec{v} + \bigtriangledown\vec{v}^{T}\right) - \frac{2}{3}\bigtriangledown\cdot\vec{v}I\right] \tag{2.3}$$

where μ is the dynamic viscosity and I is the unit tensor.

2.1.2 RANS (Reynolds Averaged Navier-Stokes) Models

Reynolds averaging consists of decomposing the solution variables in the exact Navier-Stokes equations into the mean and fluctuating components. The velocity components are [3]:

$$u_i = \vec{u}_i + u_i' \tag{2.4}$$

where $\vec{u}_i$ is the mean and u_i' the fluctuating velocity component. When this form of the flow variables is substituted into the continuity and momentum equations and a time average is taken, the ensemble-averaged momentum equations are derived. These can be expressed as:

$$\frac{\partial\rho}{\partial t} + \frac{\partial}{\partial x_i}(\rho u_i) = 0 \tag{2.5}$$

$$\frac{\partial}{\partial t}(\rho u_i) + \frac{\partial}{\partial x_j}(\rho u_i u_j) = -\frac{\partial p}{\partial x_i} + \frac{\partial}{\partial x_j}\left[\mu\left(\frac{\partial u_i}{\partial x_j} + \frac{\partial u_j}{\partial x_i} - \frac{2}{3}\delta_{ij}\frac{\partial u_i}{\partial x_i}\right)\right] + \frac{\partial}{\partial x_j}\left(-\rho\overline{u_i' u_j'}\right) \tag{2.6}$$

The Reynolds stresses, $-\rho\overline{u_i' u_j'}$, representing the turbulent behaviour, have to be modelled with the use of several turbulence models. Different turbulence models are more appropriate for different applications for which they provide different levels of accuracy.

For the case of the isolated wheel, as discussed in the Literature Review, several turbulence models have been tested. Overall, the one which provided consistently most accurate results was the *Realizable k-ε* model. Therefore, it was selected for the simulations in the present project. It is a two-equation model based on transport equations for the turbulent kinetic energy (k) and its dissipation rate (ε), which can be obtained by the following equations:

$$\frac{\partial}{\partial t}(\rho k) + \frac{\partial}{\partial x_i}(\rho k u_i) = \frac{\partial}{\partial x_j}\left[\left(\mu + \frac{\mu_t}{\sigma_k}\right)\frac{\partial k}{\partial x_j}\right] + G_k + G_b - \rho\varepsilon - Y_M + S_k \tag{2.7}$$

$$\frac{\partial}{\partial t}(\rho \varepsilon) + \frac{\partial}{\partial x_i}(\rho \varepsilon u_i) = \frac{\partial}{\partial x_j}\left[\left(\mu + \frac{\mu_t}{\sigma_\varepsilon}\right)\frac{\partial \varepsilon}{\partial x_j}\right] + \rho C_1 S\varepsilon + C_{1\varepsilon}\frac{\varepsilon}{k}C_{3\varepsilon}G_b - C_2\rho\frac{\varepsilon^2}{k+\sqrt{\nu\varepsilon}} + S_\varepsilon \tag{2.8}$$

where:

$$C_1 = max\left[0.43, \frac{\eta}{\eta+5}\right] \tag{2.9}$$

$$\eta = S\frac{k}{\varepsilon} \tag{2.10}$$

$$S = \sqrt{2S_{ij}S_{ij}} \tag{2.11}$$

In the above equations, G_k symbolizes the generation of turbulent kinetic energy caused by the mean velocity gradients and G_b the generation of turbulent kinetic energy due to buoyancy. C_2 and $C_1\varepsilon$ are constants of the model, σ_k and σ_ε are the turbulent Prandtl

numbers and S_k and S_ε are source terms.

The *Realizable* $k-\varepsilon$ model has been found to be better than the *Standard* for a wide range of flows, such as boundary layer and separated flows. The k equation is almost the same between the models, apart from the constants, but the ε equation differs, in a way that represents better the spectral energy transfer. However, the most significant difference among the *Realizable* and the rest of the $k-\varepsilon$ models is the modelling of the turbulent viscosity. It is computed from:

$$\mu_t = \rho C_\mu \frac{k^2}{\varepsilon} \tag{2.12}$$

where C_μ is not a constant and can be calculated from:

$$C_\mu = \frac{1}{A_0 + A_S \frac{kU^*}{\varepsilon}} \tag{2.13}$$

Due to these alterations, the *Realizable* $k-\varepsilon$ model might cause the production of non-physical turbulent viscosity in cases were both rotating and stationary fluid zones are used, as happens for multiple reference frames. Overall though, it has shown improved behaviour over the *Standard* model.

2.2 Rotation Modelling

An important aspect of studying an isolated wheel is the correct selection of modelling technique for its rotation since it can significantly affect the results and their accuracy. In order to be able to apply them, some modifications are also necessary for the meshing strategy. These will be described later. With the use of ANSYS Fluent, there are three main techniques for modelling the rotation of the wheel.

2.2.1 Rotating Boundary Conditions

The simplest method of applying rotation to a wall bounded flow is to set a moving boundary condition to the surface. Specifically, a rotational speed, the origin and direction of the rotation axis are set in order to complete this boundary condition [3]. For the isolated wheel, all the surfaces of the wheel, including the contact patch, were set to have a tangential rotational motion around the centre of the wheel. The application of this velocity imitates the motion of the flow around a rotating wheel, creating the appropriate boundary layer. This method does not affect the mesh and can be applied to both steady-state and transient simulations. However, it is expected to have more realistic results in cases where the rotating geometry is the same all around the axis. Therefore, more accurate results are expected at the simple-case wheel rather than the one with complicated rims.

2.2.2 Multiple Reference Frame (MRF)

The MRF method consists of modifying the equations of motion to include the acceleration terms that occur from switching from a stationary to a moving reference frame. It is an approximation of the fluid flow, but it can be reasonably accurate for many applications. When the multiple rotating reference frame is applied, a specific zone or zones are set to have a constant rotating velocity relative to the motion of the flow around these zones. The formulation of the rotating reference frame is described below. The relation of the fluid velocities are expressed by:

$$\vec{v_r} = \vec{v} - \vec{u_r} \tag{2.14}$$

where the velocity caused by the rotating frame $\vec{u_r}$ is calculated as:

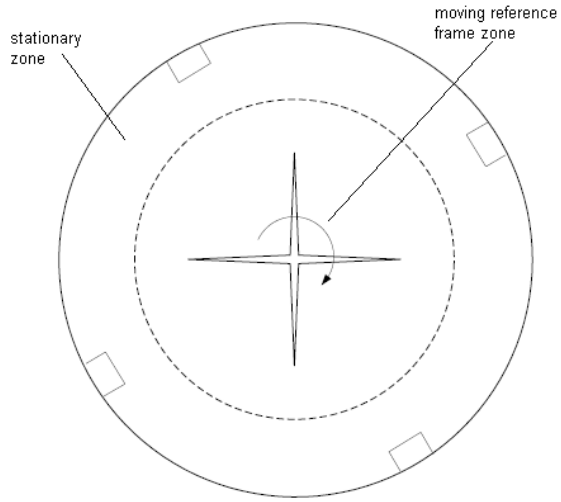

Figure 2.1: MRF [3]

$$\vec{u_r} = \vec{\omega} * \vec{r} \tag{2.15}$$

where $\vec{r}$ is the relative velocity and $\vec{v}$ is the absolute velocity. In order to solve the equations of motion in a rotating reference frame, additional terms appear in the momentum equation due to the acceleration of the fluid. The formulation of the momentum equation can be expressed in two ways, either by using the relative or the absolute velocities as dependent variables.

While this method can be used for both steady and unsteady simulations, it strongly suggested that it is only used for simple unsteady cases, since it cannot always properly calculate the strong transients that occur. The mesh remains fixed for the duration of the computation and therefore, this method does not take into account the relative motion between the moving zones and their adjacent zones.

2.2.3 Sliding Mesh

In more complex cases, where the unsteady interactions cannot be neglected, the sliding mesh model is used to incorporate the relative motion of stationary and rotating parts of the flow. It is considered the most robust method for multiple moving reference frames,

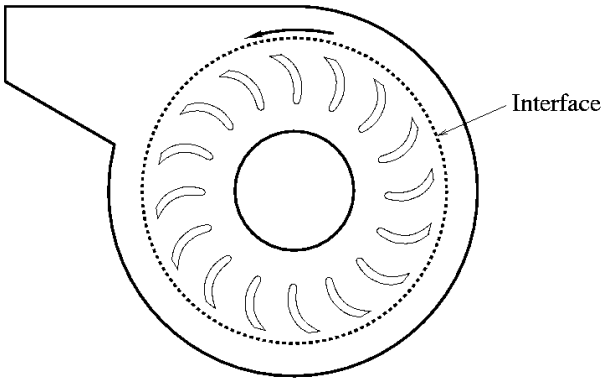

Figure 2.2: Sliding mesh method [3]

since it can also provide a time-accurate solution of the unsteady flow field, but it significantly demanding computationally.

In the sliding mesh technique, each cell zone is created independently and is bounded to the other zones by one or more ”Interfaces”, as can be seen in Figure 2.2. In this case, the rotating zone is connected to its adjacent stationary zone by one interface. During the calculation, the cell zones move relative to each other along the interface. The movement is achieved in discrete steps leading to a time-dependent solution.
Even when rotation is applied, no moving reference frames are needed, since the motion of cell zones in the computational domain is calculated based on a stationary frame. Therefore, the flux transfers through the interfaces are simplified and the relative motion between the rotating and stationary zones is tracked. The sliding mesh formulation uses

a constant control volume, so:

$$V^{n+1} = V^n \tag{2.16}$$

and the integral form of the conservation equation over a control volume, V, is expressed as:

$$\frac{d}{dt}\int_V \rho\phi dV + \int_{\partial V} \rho\phi\,(\vec{u}-\vec{u_g})\cdot d\vec{A} = \int_{\partial V} \Gamma \bigtriangledown \phi \cdot d\vec{A} + \int_V S_\phi dV \tag{2.17}$$

where ϕ is a general scalar, $\vec{u}$ and $\vec{u_g}$ are the flow velocity vector and the mesh velocity vector respectively, Γ is the diffusion coefficient and S_ϕ is the source term of ϕ. The time derivative term of the above equation can be computed using a first-order backward difference formula and since the control volume is constant this turns into:

$$\frac{d}{dt}\int_V \rho\phi dV = \frac{\left[(\rho\phi)^{n+1} - (\rho\phi)^n\right]V}{\Delta t} \tag{2.18}$$

Overall, the sliding mesh method is considered the most accurate in similar cases and thus, it was preferred over the MRF method. Furthermore, since one method is considered a continuation of the other, the comparison between the two would be counter-productive. Consequently, the rotation methods to be compared in the present project are simple rotating boundary conditions and the sliding mesh method.

2.3 Overset Mesh

Overall, the sliding mesh method is considered the most accurate in similar cases and thus, it was preferred over the MRF method. Furthermore, since one method is considered a continuation of the other, the comparison between the two would be counter productive. Consequently, the rotation methods to be compared in the present project are simple rotating boundary conditions and the sliding mesh method. 2.3. The background mesh is

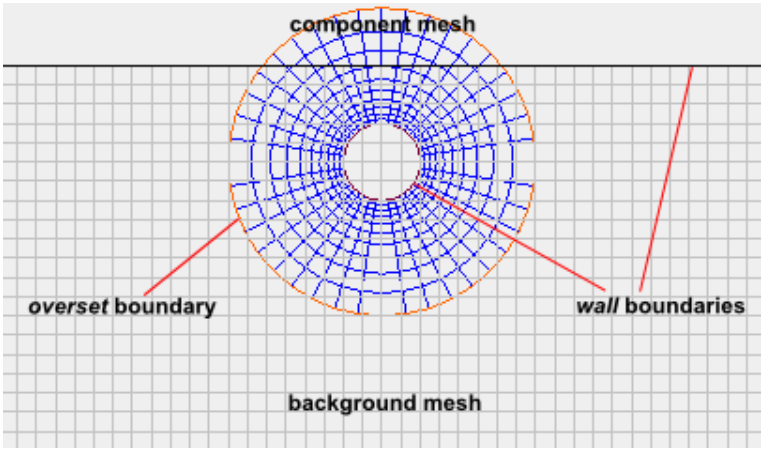

Figure 2.3: Overset mesh method [3]

the main area or volume where the simulation is set, while many component meshes can be added in order to acquire the necessary topology. The outer physical boundaries of the domain are set by the background mesh since the outer boundaries of the component meshes must have the boundary condition ”Overset”. The overset mesh method has some limitations which are going to be described later, especially in Fluent, where it is relatively new. It is important to note that it has not yet been used for applications including wheels.

2.4 Geometries

- **Baseline Geometry**

  Initially, a widely studied geometry was needed in order to properly validate the results. Therefore, the experiments performed by Fackrell [17] was considered ideal. In those experiments, the wheels were set to rotate freely in bearings, while in contact with a moving floor. It was supported in that position by a system of adjustable rods, while in order to acquire pressure data around the wheel's circumference, pressure sensing holes were needed on its surface. Several arrangements were made to eliminate any centrifugal effects, but it was confirmed that the equipment could detect all the detailed fluctuations that occur rapidly. The sampling for the pressure data was conducted for a full revolution of the wheel, while mean pressure distributions were also stored.

  There have been numerous studies referring to Fackrell's geometry and expanding knowledge on the topic of isolated wheels. In the experiment 2 different tyre profiles and 3 different widths were combined to produce 6 test cases.

  Over more recent studies, one of these cases has mostly been revisited and it was called the *A2* geometry. It is presented in Figure 2.4a and it consists of a simple wheel without any deformation or treading on the tyre, while the rim area is significantly simplified. The CAD geometry of the baseline model as seen in Figure 2.4a was created using CATIA. The wheel is asymmetric and its main geometrical characteristics are:

Total Diameter	0.416m
Rim Diameter	0.3285m
Outer Width	0.1906m
Inner Width	0.0175m

Table 2.1: Geometrical characteristics

The flow characteristics as described by Fackrell are presented in Table 2.2 and they have been chosen in order to accurately represent the real flow around the wheel of a racing car.

Test speed	$18.6m/s$
Reynolds number	$5.3x10^5$
ρ	$1.225km/m^3$

Table 2.2: Flow characteristics

This simplified model was used for validation of the initial calculations, and also as a base for the modifications that were made later. These modifications aimed at complicating the geometrical characteristics of the wheel and consequently the flow around it. The changes that were made, were based on realistic wheels since some of their characteristics were imitated. Those were the addition of grooves and a more realistic rim geometry.

- **Grooved Tyre**

The grooves that were added to the surface of the tyre are widely used in production vehicles, while their geometry is also very close to the one used by Fackrell. The depth of the grooves was set to $3mm$ and the width to $5mm$. In Fackrell's experiments, the width was larger, since the effects of their existence needed to be exaggerated in order to be more easily detectable. However, for the present project, a more realistic approach was selected. The resulting geometry can be seen in Figure 2.5a.

- **Wheel with rim**

  The rim geometry design was intended to provide a more complex geometry that would alter the flow in that area. Consequently, differences in the wake region and around the wheel would be detected and the rims could be isolated as the main cause for the new flow structures. A simple geometry was used to assist the meshing process, but it was also considered sufficiently realistic regarding its effect on the fluid flow. The geometry of the rims can be seen in Figure 2.5c.

- **Grooved Tyre with Rim**

  Subsequently, after the grooves and the rims were added separately to the geometry, another case which included both of these modifications was created. The investigation of the most complex geometry including realistic rims and grooved tyres was also significant, since it presents the most similarities with wheels used in actual automotive applications. The exact geometry is shown in Figure 2.5c.

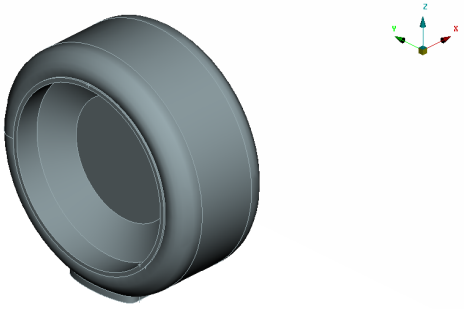

(a) Baseline wheel geometry [17]

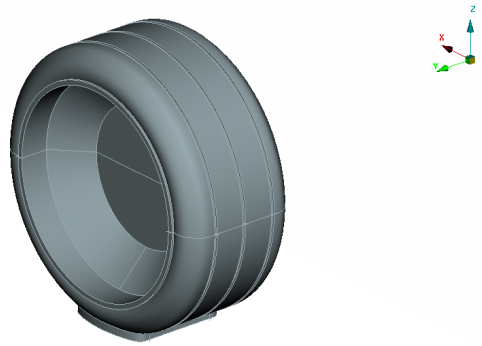

(a) Grooved tyre geometry

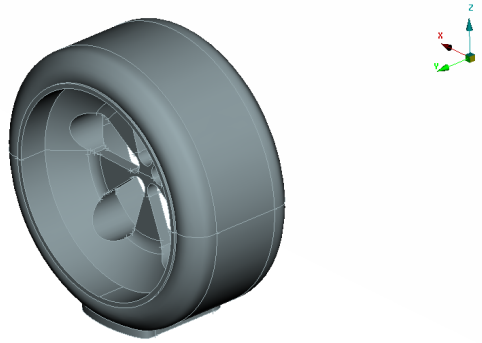

(b) Wheel with rim geometry

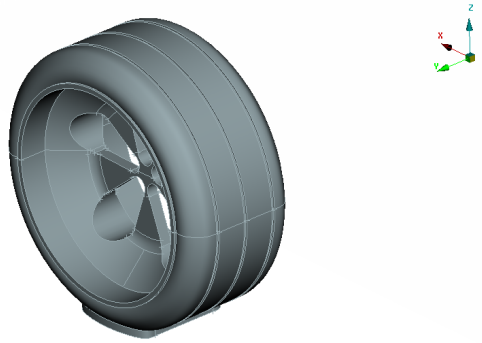

(c) Grooved tyre with rim

Figure 2.5: Tyre geometries

- **Wheel with Camber Angle**

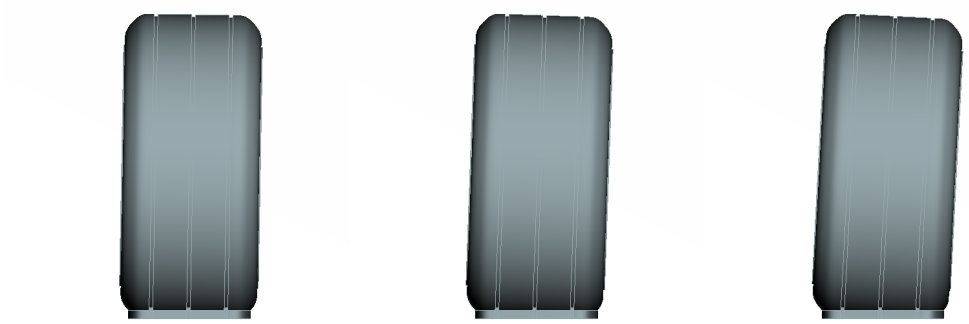

(a) -1^o (b) -2^o (c) -3^o

Figure 2.6: Camber angles

One of the above geometries was needed in order to investigate the effects of the wheel's camber angle. The baseline wheel was considered overly simple to reveal any slight changes of the flow structures. On the other hand, the geometry with the complex rims would cause significant alterations in the flow, impeding the detection of any newly created phenomena. Therefore, the grooved wheel was chosen to be tested under different camber angles as a more realistic approach, which would enhance any distinct flow features.

The values of the angles follow the typical values that are used in the automotive industry and are in the range of what has been previously used in literature [35], [36], [37]. The exact models, with angles of $-1°, -2° and -3°$ respectively are presented in Figure 4.9.

- **Wheel with Different Step Heights**

The effect of the step size on the behaviour of the flow was investigated using the baseline wheel model. The step size was set by altering the height, while the other dimensions changed accordingly, as has been previously done in the literature

[1]. The height ranged from 1.5*mm* to 15*mm* or 0.36% to 3.6% of the wheel's diameter. All heights that were tested for this project can be seen below, in Table 2.3. The height was not the only dimension that changed in each case, since the

Height (mm)	**Height (% of diameter)**
1.5	0.36
2.5	0.6
5	1.2
7.5	1.8
10	2.4
12	2.885
15	3.6

Table 2.3: Step heights

circumference of the wheel at each specific height was extruded towards the ground. Figure 2.7 shows the difference between the smallest and the largest heights.

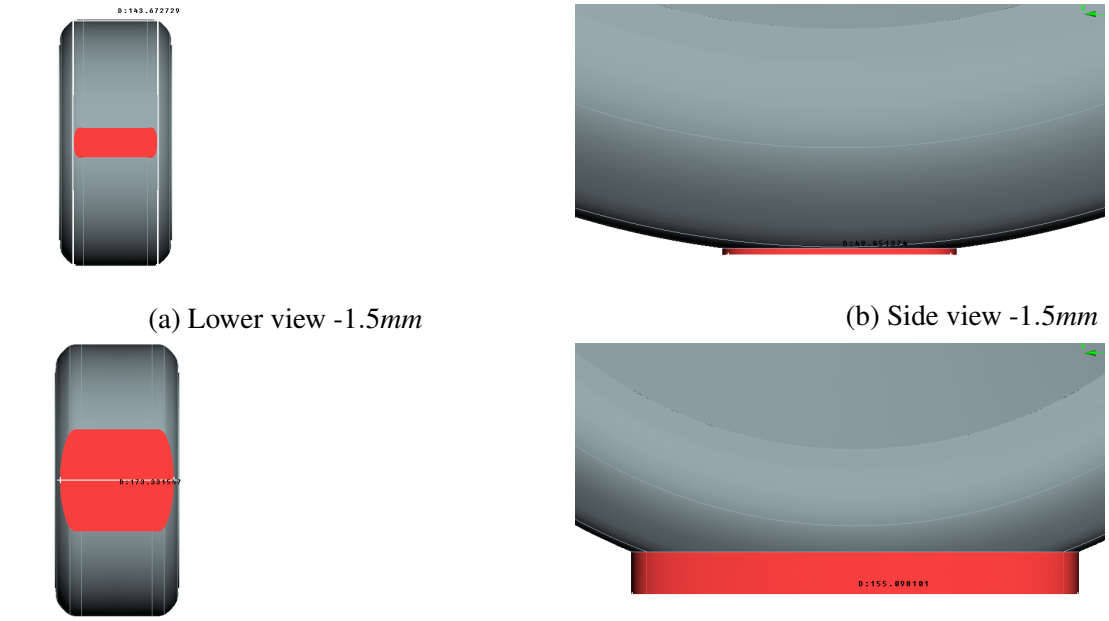

(a) Lower view -1.5*mm*

(b) Side view -1.5*mm*

(c) Lower view -15*mm*

(d) Side view -15*mm*

Figure 2.7: Effect of different step heights on wheel geometry

2.5 Grid Generation Strategy

The software ANSA by BETA CAE Systems was used for the mesh generation of all different cases. The overall strategy was focused on building a surface mesh that consists of triangular elements, while prismatic cells comprise of the boundary layer. The rest of the domain is filled with tetrahedral elements. This setup was kept simple, so that it could be applied in both initial generic geometries, as well as the more complicated that followed. Furthermore, the unstructured nature of these grids allowed for fewer overall elements, leading to smaller computational costs. It was considered important to keep a consistent grid generation strategy during the whole project, but some slight differences were essential in order to apply the rotation models that were described above. These differences concern mainly the grid around the wheel and thus, will be explained in the respective section below.

2.5.1 Computational Domain

The selection of the computational domain is vital for external aerodynamic analyses, since the size can significantly affect the results. If not chosen correctly, it can alter the fluid flow around the wheel and disrupt the formation of different structures in the wake or above the wheel. The maximum dimensions of all the test cases were the same, therefore the size of the outer control volume also remained identical for all the simulations. After considering previous studies, the domain size used by McManus [2] was preferred, since the objectives of that study were particularly similar, as Fackrell's [17] work was also referred to and the flow around an isolated wheel was investigated. Therefore, the domain extends 5 diametres in front of the wheel, 15 diametres behind it and 2.93 above it, while the width of the domain is 1.523m. The whole model can be seen in Figure 2.8 where the wheel is also located inside the domain for scale. The mesh on the surface of the ground

ranged from 40mm to 80mm according to the needed density of the mesh, while for the rest of the outer domain the size was between 50mm and 110mm.

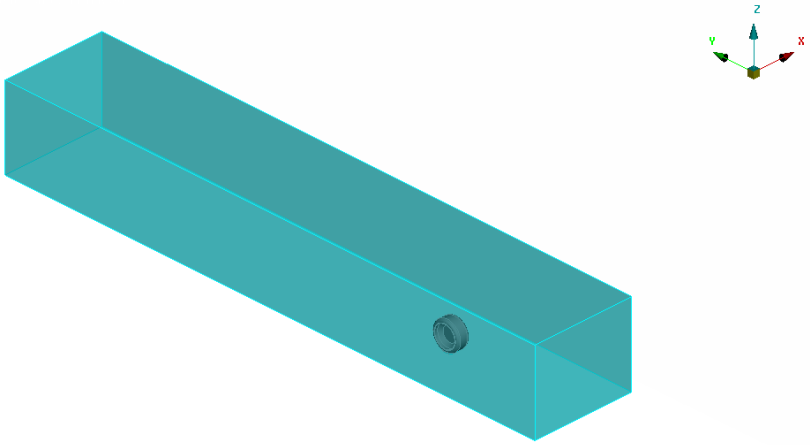

Figure 2.8: Computational Domain

2.5.2 Wheel

As described previously, the surface mesh on the wheel is triangular and it ranges between 1mm and 5mm for the medium mesh. The strategy that was chosen for the creation of the boundary layer, was to use a $y+$ of 30 while also applying Wall Functions. It has been noticed from previous studies [28], [23], [14], [27] that, even with the use of wall functions, trustworthy results can be produced with most turbulence models. Thus, it was concluded that the use of a higher $y+$ of 30, as mentioned above, would be sufficient regarding the outcomes and also would make it easier to keep a lower number of elements, minimising the computational cost. Therefore, the boundary layer consists of 7 elements normal to the wheel, where the 2 last ones have a larger growth ratio in order to make the transition to the bigger tetrahedral elements smoother. This can be seen in detail in Figure 2.9.

Another important aspect of modelling a wheel is the area around the contact patch. The most widely used and easiest to apply is the creation of a ”step” around the base of the

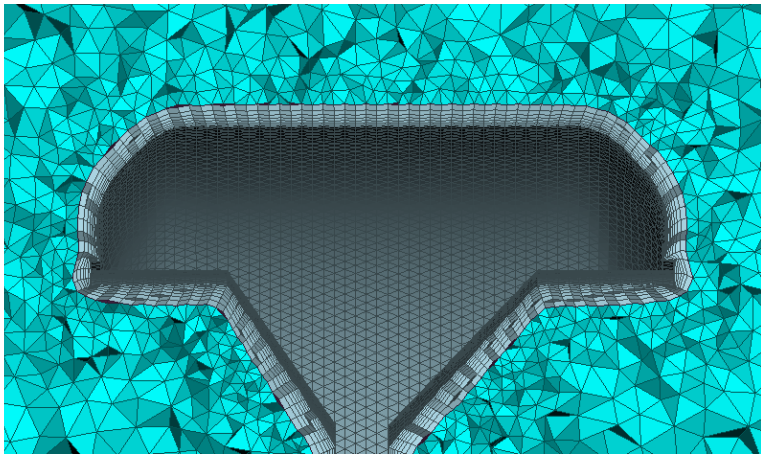

Figure 2.9: Transition from prismatic to tetrahedral elements

wheel. The height of this ”step” must be large enough in order to be able to have good quality elements, but small enough to not alter the flow around the contact patch significantly. For this case, a height of 12*mm* was chosen, which is approximately 2.88% of the wheel's diameter and can be seen in Figure 2.10.

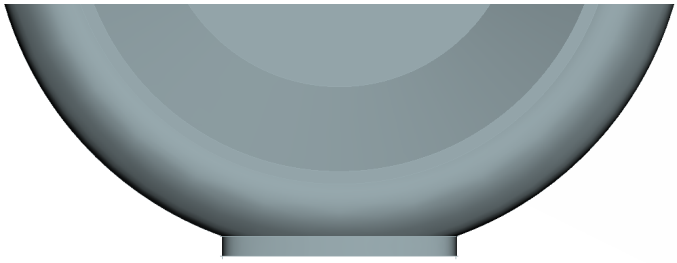

Figure 2.10: Contact patch

The setup that was described above is the main that was applied in all cases and details of the rest of the grids can be found in the appendix. However, the sliding mesh technique requires some extra modifications in the meshing strategy. The main additional characteristics that were needed were the interfaces at the sides of the wheel. They were required in order to isolate the left and right volumes at the rim area, which rotate when the sliding

method is used. The same was applied even in the case with the more realistic rim, but the rotating area was just one instead of one on each side. Both of these altered geometries are presented in Figure 2.11.

(a) Baseline rim (b) Realistic rim

Figure 2.11: Sliding mesh geometry

2.6 Overset model and mesh

The overset method required a different approach regarding the creation of the model and the meshing strategy, which are going to be described in more detail in this section. As mentioned previously, the overset technique in Fluent allows for independently generated grids to be computed as one continuous mesh. This provides a great advantage in complicated geometries, since each part can be meshed isolated, removing several local constraints that might occur. For the case of the isolated wheel, this method could be used in order to eliminate the need for a ”step” on the contact patch region, while still retaining good quality elements in that area. Therefore, the initial concept behind the use of the overset technique, was to keep the outer boundaries of the domain which would form the background mesh. The component mesh would consist of a small area around the wheel, but would also exceed the outer boundaries of the control volume, as shown in Figure 2.12.

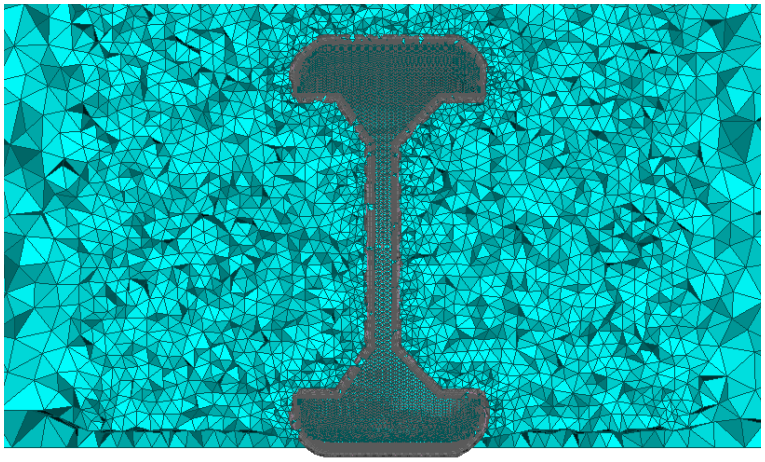

Figure 2.12: Initial concept of overset topology

However, there are some limitations when it comes to building the overset topologies, the most important of which is that physical boundaries, such as those on the ground and the wheel surface, cannot intersect with each other. For the case of the isolated wheel, the two surfaces should only overlap, which under some circumstances is acceptable in Fluent. However, due to the cylindrical profile of the wheel, this geometry was not acceptable or applicable for the overset method, since the surfaces were always considered as overlapping. Thus, it was attempted to overcome this issue, by trying different meshing strategies. The most successful one will be presented further in this thesis. With this approach, it was intended to keep the wheel above the ground level, not overlapping or intersecting, but as close as possible to its correct position. However, another restriction was set in this case since there should be at least 4 cells between the physical boundaries, so that the interpolation among the two grids can be achieved correctly. Consequently, the most successful mesh that followed this logic includes the wheel located 5mm above the ground level, while the component mesh consists only of the prismatic boundary layer.

With the approach described above, it was made possible to perform steady state simulations with converged results, which are going to be presented in the next chapter. Since

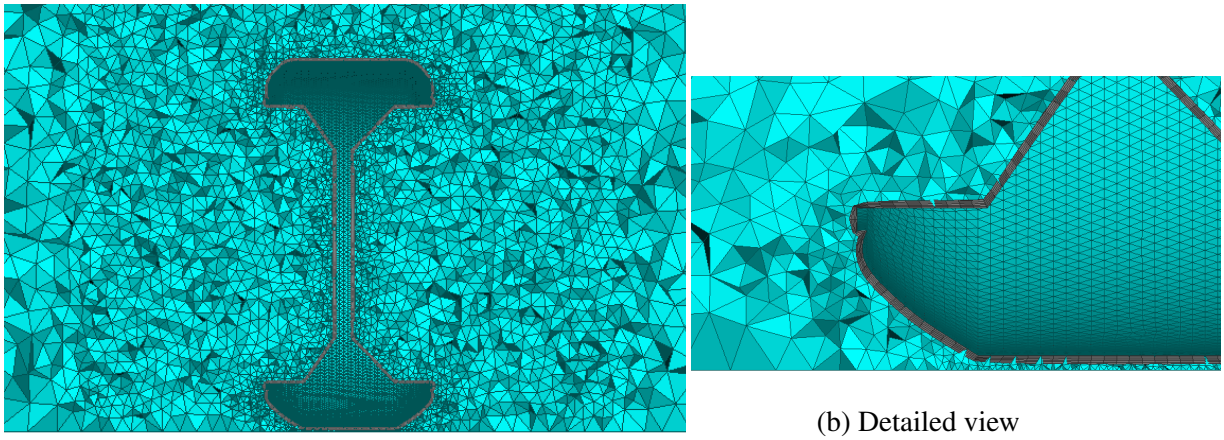

(a) Overset topology

(b) Detailed view

Figure 2.13: Overset mesh

the channel created at the bottom alters the flow significantly, the results are not expected to be particularly accurate, but it is important to be able to compare to this method that has not been used before for similar cases.

2.7 Solver Setup

In the following section, all the parameters that were set in Fluent will be described and justified. Several settings were kept the same during the whole project, while others changed according to the respective type of simulation.

2.7.1 Boundary Conditions

The boundary conditions that are shown in Table 2.4 were applied for all the calculations. They were chosen based on McManus' case [2], which studied the same initial geometry with great success, since those results were very close to the experimental.

The exact surfaces where those boundary conditions were applied, can also be seen in Figure 2.14

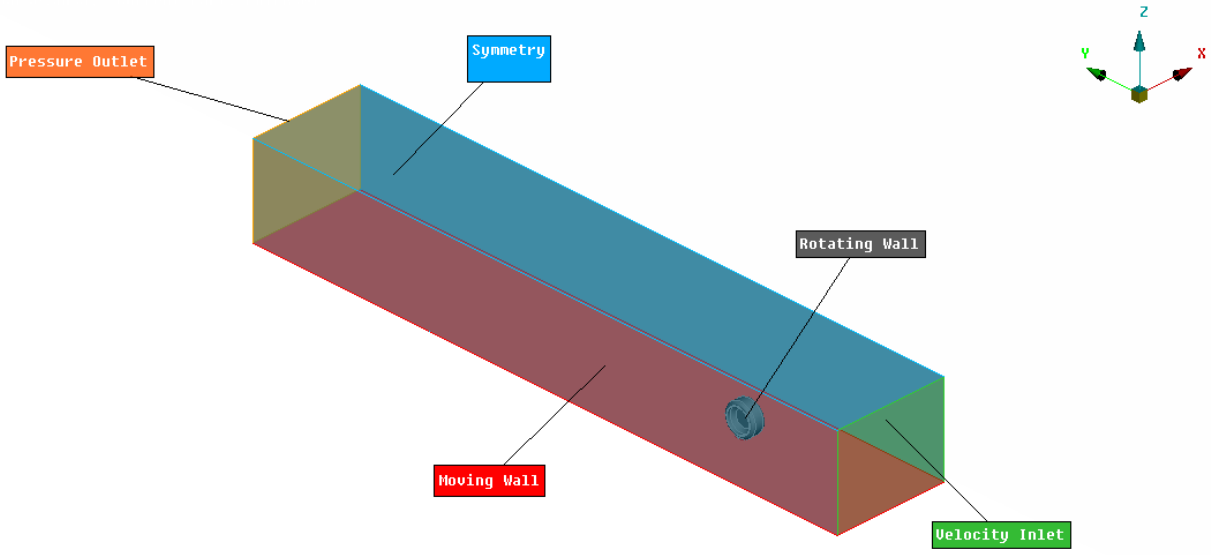

Figure 2.14: Boundary Conditions

Boundary	Applied Boundary Condition
Inlet	Velocity inlet: $18.6 m/s$ Turbulent intensity: 0.2% Hydraulic diameter: $1.35m$
Outlet	Pressure Outlet
Top and Side walls	Symmetry
Ground	Moving wall with $v = 18.6 m/s$
Wheel (including contact patch)	Rotating wall with $\omega = 89.44 rad/s$

Table 2.4: Boundary Conditions

2.7.2 Turbulence Model and Numerical Methods

As mentioned previously, the *Realizable* $k-\varepsilon$ turbulence model was used for this project. It has proved to be especially accurate for similar cases [12], [2], [27], [28] when also being combined with the use of Standard Wall Functions.

The pressure-based solver was used for all the simulations. In ANSYS Fluent, pressure-velocity coupling is used to derive an additional condition for the pressure by using an alternative formation of the continuity equation. For the present project the default op-

tion, which is the SIMPLE algorithm, was applied since the case was relatively simple a convergence problem was expected to occur. The SIMPLE algorithm utilises a relationship among pressure corrections and velocity to obtain the pressure field for each iteration. Initially, the momentum is solved with a guessed pressure field, resulting in a flux correcting equation, which is then substituted into the continuity equation. The pressure correction is derived and solved to come up with the corrected cell pressure and flux. The spatial discretisation of the pressure and momentum is achieved through the second order Upwind scheme for all cases. The turbulent kinetic energy and the turbulent dissipation rate use the first order scheme only for the meshes that are needed for the grid convergence study. Thus convergence was reached faster, while it was noticed that the accuracy was not affected. The convergence criteria for the steady-state simulations were set to 10^{-5}, while the solution was considered stable when there was no obvious change in the residuals for at least 2000 iterations.

2.7.3 Overset mesh setup

The solver setup for the overset mesh differs slightly from the previous, since not all options available in Fluent are yet supported for this method.

Firstly, the *Standard* $k-\varepsilon$ turbulence model had to be used, since the *Realizable* is not supported for overset meshes. The differentiation between the two is in the calculation of turbulent viscosity. Initially, the transport equations are expressed as:

$$\frac{\partial}{\partial t}(\rho k)+\frac{\partial}{\partial x_i}(\rho k u_i)=\frac{\partial}{\partial x_j}\left[\left(\mu+\frac{\mu_t}{\sigma_k}\right)\frac{\partial k}{\partial x_j}\right]+G_k+G_b-\rho\varepsilon-Y_M+S_k \tag{2.19}$$

$$\frac{\partial}{\partial t}(\rho \varepsilon)+\frac{\partial}{\partial x_i}(\rho \varepsilon u_i)=\frac{\partial}{\partial x_j}\left[\left(\mu+\frac{\mu_t}{\sigma_\varepsilon}\right)\frac{\partial \varepsilon}{\partial x_j}\right]C_{i\varepsilon}\frac{\varepsilon}{k}(G_k+C_{3\varepsilon}G_b)-C_{2\varepsilon}\rho\frac{\varepsilon^2}{k}+S_\varepsilon \tag{2.20}$$

where the turbulent viscosity is also computed by Equation 2.13, but C_μ is a constant.
Another significant differentiation among the simulations will be the use of the *Coupled* pressure based solver. In contrary to the segregated solvers, it solves the momentum and pressure-based continuity equations together. The pressure gradient terms in the momentum equations, as well as the face mass flux, are discretised implicitly, making the full implicit coupling possible.
Overall, these changes might have an effect on the accuracy of the results, but they are not expected to significantly alter them.

2.7.4 Time-dependent Simulations

As mentioned previously, the sliding mesh method is inherently transient, and thus, several extra parameters had to be calculated in order to perform unsteady simulations. The timestep was calculated through the characteristic velocity and time for this case, which were set as the inlet velocity and wheel diameter. Specifically:

$$T_c = \frac{0.416}{18.6} = 0.02237s$$

$$dt = 0.0001s$$

$$N = 7000$$

$$T = 0.7s$$

Furthermore, extra data was needed to reach conclusions regarding the flow field. However, since the flow is not stable from the beginning of the simulation, this data is collected afterwards. Specifically, the simulation was set to run for 2 wheel rotations, or 0.28sec, without collecting any data, while all the data was averaged for the next 3 rotations, or 0.42sec. This was considered enough to have an accurate average for the needed variables.

Chapter 3

Preliminary Study

The preliminary study consists of the simulations performed in order to validate the initial setup and to set the most appropriate characteristics for the rest of the project. The baseline geometry, as described previously, was used, while three different grid levels were tested. A grid convergence study was conducted and all the parameters will be presented below. These initial simulations were performed with rotating boundary conditions on the wheel, but the same overall setup was also used for the sliding and overset mesh method. Therefore, the results for those are also going to be presented in this chapter.

Although previous studies have shown that this case is not significantly grid dependent, it was important to specify an appropriate grid size for the initial case. Therefore, the three different levels were tested under the same conditions. The grid generation strategy was the same for all levels, differentiating the cell sizes according to the needed density.

3.1 Grid Convergence Study

The quantification of the confidence level of the performed simulations can be achieved through the well–known GCI (*Grid Convergence Index*) method. It was introduced in

1997 by Roache in [38] and it aims in proving the monotonic reduction of the discretisation error by refinement of the mesh. Specifically, three different grid levels were considered, as seen in Table 3.1. The approximate refinement ratio r is considered

$$r = \frac{\Delta x_2}{\Delta x_1} = \frac{\Delta x_3}{\Delta x_2} \approx 2 \tag{3.1}$$

and the grid refinement study is performed by computing the drag and lift coefficients, C_D and C_L for the different meshes shown in Table 3.1.

#	Mesh	Elements
1	fine	$4.9 \cdot 10^5$
2	medium	$9.91 \cdot 10^5$
3	coarse	$19.92 \cdot 10^5$

Table 3.1: Three grid levels

Considering as f the computed coefficient, either C_D or C_L, the *observed order of accuracy* is

$$\gamma = \frac{\ln\left(\frac{f_3 - f_2}{f_2 - f_1}\right)}{\ln(r)}, \tag{3.2}$$

Subsequently, the relative differences between the solutions of coarse and medium and between medium and fine meshes are calculated as

$$\varepsilon_{1,2} = \frac{f_1 - f_2}{f_1} \quad \text{and} \quad \varepsilon_{2,3} = \frac{f_2 - f_3}{f_2}. \tag{3.3}$$

Then, the Grid Convergence Index (GCI) is expressed for the two levels as

$$\mathrm{GCI}_{1,2} = \frac{F_s|\varepsilon_{1,2}|}{r^\gamma - 1} \quad \text{and} \quad \mathrm{GCI}_{2,3} = \frac{F_s|\varepsilon_{2,3}|r^\gamma}{r^\gamma - 1}, \tag{3.4}$$

where F_S is a safety factor with a recommended value of 1.25 for three grid levels. (ROACH) If all the values of f are in the asymptotic range of convergence, showing also

a monotonic reduction in the discretisation error, then the following expression should be satisfied.

$$GCI_{2,3} = r^{\gamma} GCI_{1,2}. \tag{3.5}$$

Therefore the following ratio has to be approximately equal to 1.

$$\mathscr{R} = \frac{GCI_{2,3}}{r^{\gamma} GCI_{1,2}} \approx 1. \tag{3.6}$$

The lift and drag coefficients that were acquired by the three different grid levels with a considered refinement ratio of 2 can be seen in Table 3.2, while Table 3.3 shows the values of all the variables that were previously described for the grid convergence study. The convergence was investigated for both variables C_L and C_D, since they were considered equally important at this stage. The computational time is given as a function of the time required for the shortest simulation which was the one performed for the coarse mesh.

		C_L	C_D	Computational time
1	fine	0.2624	0.4749	1
2	medium	0.2659	0.4767	2.42
3	coarse	0.2703	0.4802	5.74

Table 3.2: Lift and Drag Coefficient using different mesh levels

For both force coefficients, the ratio R is approximately equal to one, thus satisfying equation 3.5. Therefore, the values of lift and drag coefficients are in the asymptotic range of convergence.

It is also possible to conclude that this case is not significantly grid dependent, since all the computed values of the forces' coefficients were very close, even though the grids had vastly different sizes. This has also been noticed in previous studies, but this characteristic

	γ	ε_{12}	ε_{23}	GCI_{12}	GCI_{23}	$\mathscr{R}$
C_L	0.3301	-0.0133	-0.0166	0.0648	0.0804	0.9869
C_D	0.9594	-0.0038	-0.0073	0.005	0.0097	0.9962

Table 3.3: Grid converge index analysis

does not apply to more complicated cases, such as the ones that will be described in the next Chapter. Therefore, it is important to decide on the most appropriate grid based on its results and characteristics. The results of the medium grid are almost identical to the ones of the fine grid, with a fraction of the computational cost. Therefore, the strategy for the creation of the medium grid can be considered the most appropriate and should be used for future geometries and simulations.

3.2 Clustered Grid

As it has been proven above, convergence of the results occurs with the refinement of the mesh, not only on the wheel's surface, but also on the surrounding area. The medium and the fine meshes have a more dense grid only on the surface of the wheel and surrounding area. However, for the present project, the flow structures around a greater region, such as the wake, are important. Thus, it was decided to create a grid with the parameters of

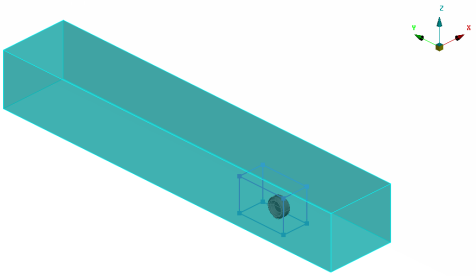

Figure 3.1: Refinement area

the medium mesh for the surface, but with a refinement area around it. This region can be seen in Figure 3.1 and was used in all the cases after the Grid Convergence Study.

3.3 Pressure Distribution

The pressure distribution on the surface of the wheel was one of Fackrell's most important results, since it can show flow features and phenomena, and have been for most researchers the main aspect of comparison to that study. The pressure coefficient on the circumference of the wheel's centreline will be presented as a function of each point's location around the wheel, as was performed in the original study. The positions of the points are as shown in Figure 3.2a.

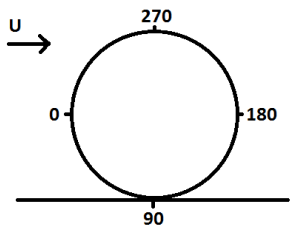

(a) Point positioning

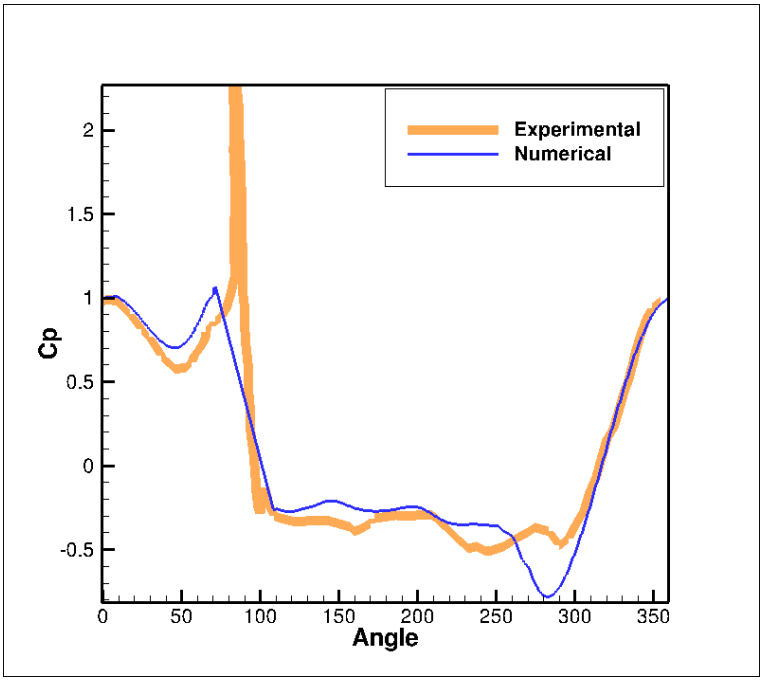

(b) Pressure coefficient comparison along centreline

Figure 3.2

Overall, the results represent the flow features relatively well, although the highest values of pressure are significantly underestimated, because of the existence of the contact patch. The pressure at the front part of the wheel, where the flow is accelerated is computed quite accurately. However, at the separation area, at around 270^o, the values of

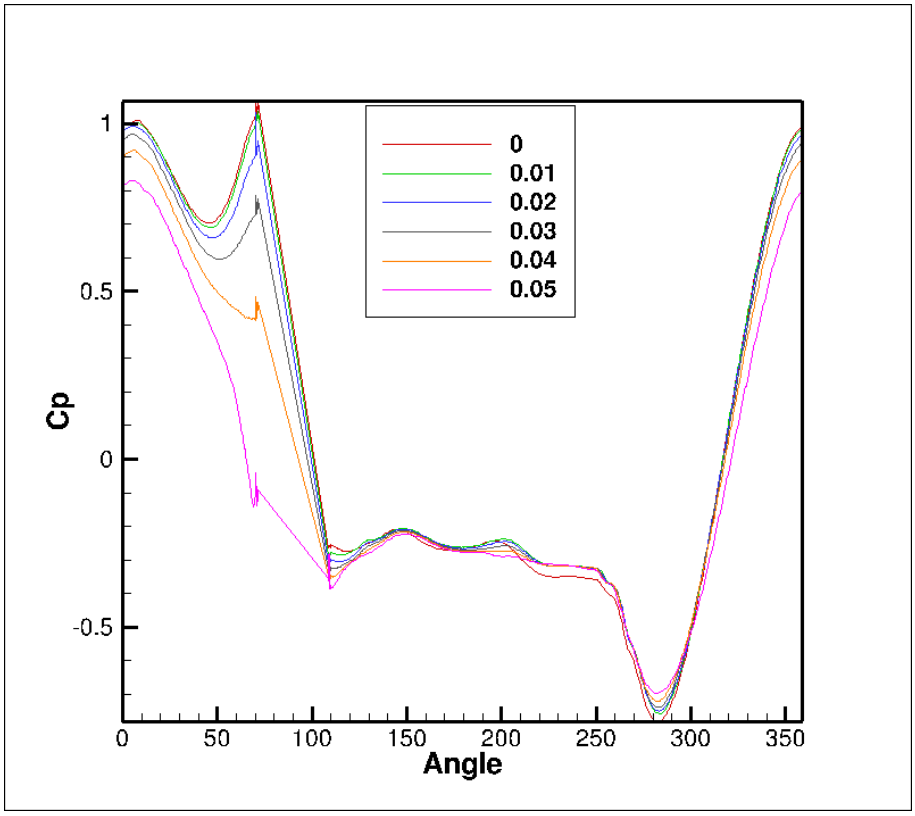

Figure 3.3: Pressure coefficient on different lines along the wheel's circumference

the computed pressure are lower than the experimental. This phenomenon has also been noticed in previous research and is assumed to occur because of CFD not being able to handle separation accurately. The pressure distribution in different areas of the wheel was also investigated and is shown in Figure 3.3. Apart from the centreline, the rest of the locations chosen were 0.01m, 0.02m, 0.03m, 0.04m and 0.05m away from the centreline accordingly. Since the results are averaged over time, the distribution is symmetrical and thus, there was no need to provide data for both sides. The results show that the pressure is the highest along the centreline and gradually decreases when moving closer to the sides. This effect is most intense around the contact patch, where the C_P changes abruptly, and also for other locations of high pressure, such as the the areas around 0^o. The separation, with very low C_P values, seems to be exaggerated in the whole width of the wheel.

3.4 Error Calculation

Subsequently, the L_0, L_1 and L_2 errors for the pressure distribution on the centreline were calculated in order to estimate the accuracy of the different grids. The errors for each grid are presented in Table 3.4. The L_0 error is great, as expected, since the maximum

Grids	L_0	L_1	L_2
Coarse	1.7138	0.3022	0.2884
Medium	1.7077	0.2998	0.2854
Fine	1.6805	0.2970	0.2744
Clustered	1.6877	0.2989	0.2782

Table 3.4: C_P Errors

values of the computed C_P are much lower than the experimental. The L_1 and L_2 errors are comparable and quite low, proving that the results are overall accurate. The errors are slightly reduced with the refinement of the meshes, but the difference in value is not great. The Clustered mesh that was used for most of the simulations is in general slightly worse than the fine, but significantly better than the medium.

3.5 Sliding Mesh

The sliding mesh method was used for the clustered mesh. Two different grid levels were tested for this case. The simulations run for 7000 timesteps, but for almost the first 3000 the flow was not completely stable. The history of C_D and C_L were considered to prove if the flow has become completely stable. These can be seen in Figure 3.4. The coefficients have extreme values at the beginning of the simulations, but slowly they become stable and they oscillate around the same values depending on the progression of timesteps and the specific moment in the rotation. The coefficients for other simulations will be provided in the Appendix. In order to provide quantitative data for comparison with the

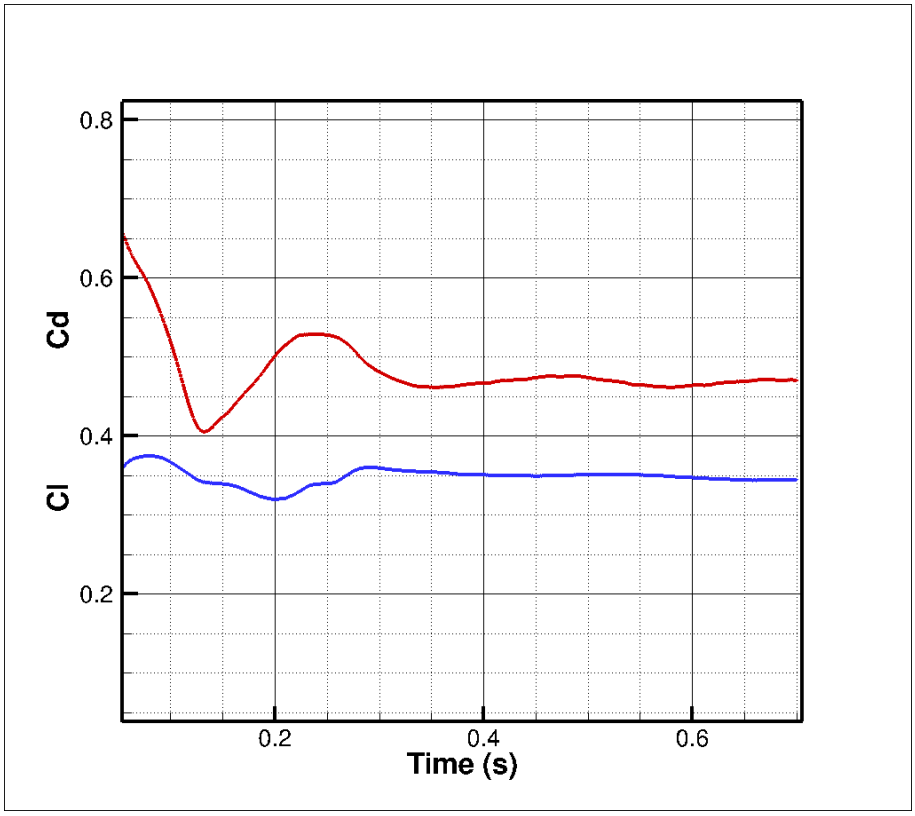

Figure 3.4: C_D and C_L over time

previous simulations, the averaged C_D and C_L over three wheel rotations were calculated. The relative errors for all the cases are presented in Table 3.5. The Matlab code for the calculation of the error norms can be found in the Appendix. The results significantly

Cases	C_D	C_D error	C_L	C_L error
Coarse Sliding	0.46936	1.29%	0.31	10.71%
Medium Sliding	0.50344	7.97%	0.27	3.57%
Experimental	0.51	-	0.28	-

Table 3.5: C_D and C_L and relative errors

improve for the medium sliding mesh. However, the coarse mesh was not as accurate, proving that the method depends on grid refinement. Considering the high computational cost of sliding meshes, their use is only suggested in finer grids. If highly accurate results are needed, it makes it possible to provide more data that is also trustworthy.

3.6 Overset Mesh

The overset method was used with the parameters that were described in the second chapter, while the wheel was located 5*mm* above the ground level. Firstly, the forces coefficients are presented in Table 3.6. As it was expected, the lift coefficient is negative, since

	Overset mesh
C_D	0.6101
C_L	-0.239

Table 3.6: C_D and C_L for the overset mesh

a channel exists between the wheel and the ground. The downforce that is applied on the wheel is caused by the Magnus effect that occurs on rotating cylindrical geometries. This negative lift force affects the drag coefficient raising its value. The C_D is much higher than the experimental, but it is still comparable to the previous numerical results. Therefore, it is important to observe the flow field around the wheel to identify the phenomena and their similarity with the baseline case. Thus, total pressure contours were created on the central plane of the domain and are presented in Figure 3.5. Overall, the flow field is very similar to the initial case, but the wake is significantly smaller. The separation point is moved rearward, thus increasing the drag, while the separation area is moved closer to the wheel. However, the flow field is particularly detailed for a steady state simulation. The overset mesh method as it exists now in Fluent is not appropriate for this specific case. The results, although not greatly different than the experimental, are not trustworthy in order for the technique to be used as the main simulation method for future research. If the restriction on the overlapping physical boundaries is raised, then the overset mesh will be able to provide significant improvements on the realistic representation of this problem.

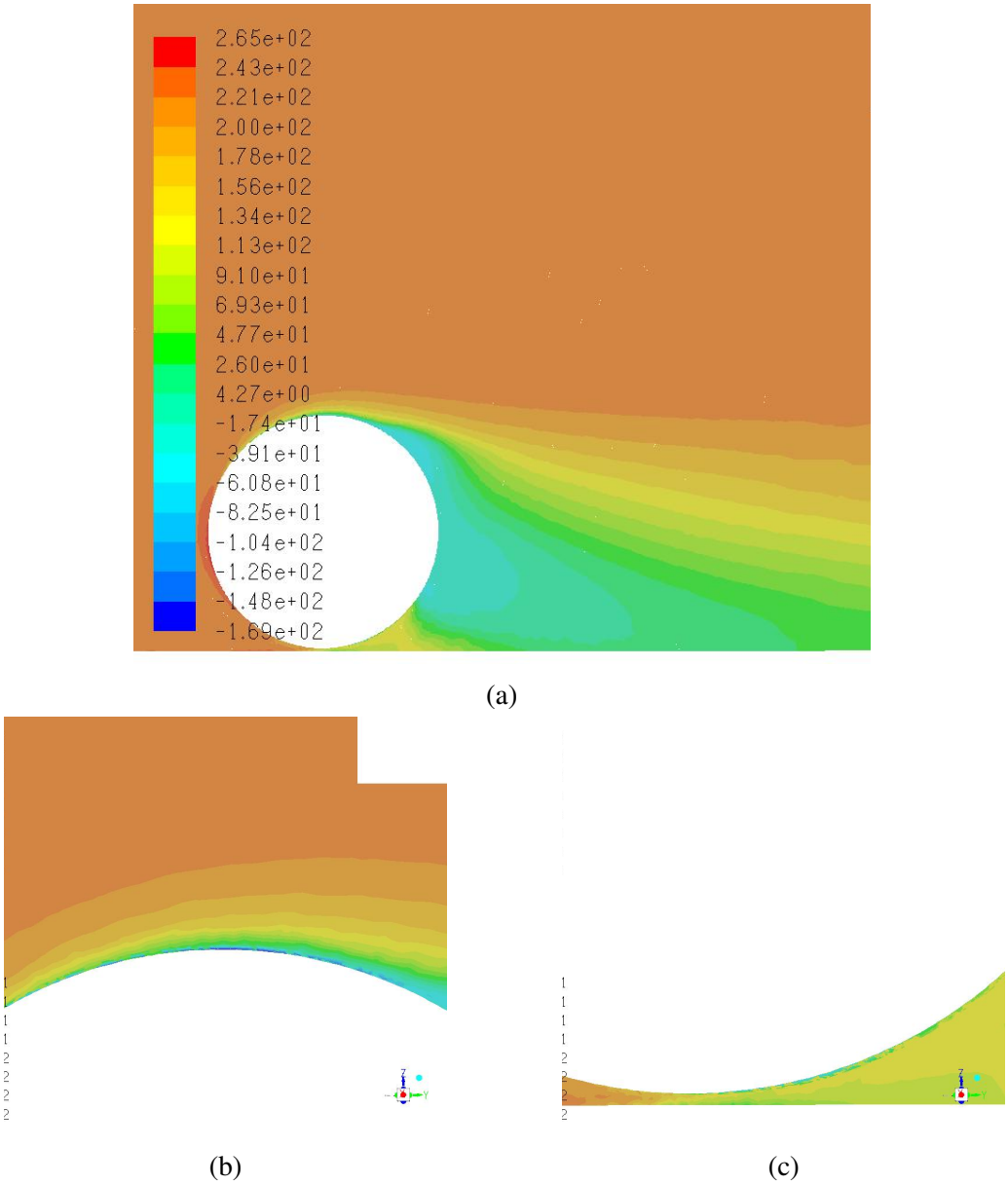

(a)

(b) (c)

Figure 3.5: Total pressure along the central plane

3.7 Flow Field

Apart from the quantitative data that has been presented, it is important to examine the qualitative results in order to verify the existence of certain flow phenomena. The analysis of the flow field included the investigation of the vortical structures around the wheel.

Over these regions, the *Q criterion* was used to identify three-dimensional vortices [39]. The *Q criterion* consists of the second invariant of the velocity gradient tensor and can be expressed as:

$$Q = \frac{1}{2}\left[tr(J)^2 - tr(J \cdot J)\right] \tag{3.7}$$

where $tr()$ is the trace of a matrix and J represents the Jacobian tensor of the velocity. Q has proven to be able to show successfully three dimensional vortices. Isosurfaces of the *Q criterion* are used for this project and the value used each time will be mentioned in the respective section.

For the baseline wheel, C_P contours over the centreline of the domain along with streamlines are presented in Figure 3.6. The highest values of pressure are located at the front of the wheel, especially at the contact patch area. The flow at the wake is characterised by the great separation area at the top and rear of the wheel. The recirculation area is large in that region, while a smaller vortex is located right behind the contact patch. The part of the wake where the flow phenomena are stronger is approximately one diameter long. The separation of the flow occurs at a location very close to the top of the wheel and it gets reattached farther at the wake.

The vortices can be detected properly in Figure 3.7, where isosurfaces of $Qcriterion$ equal to 2500 are shown. The two counter rotating vortices at the lower part of the wheel are the strongest phenomena that can be seen in the wake area. The separation area at the top is also eminent, while there is also a great vortical region at the rim area. This is connected to the ground plane through the contact patch, where the start of the small vortex at the near wake is located. Overall, the flow features that were expected can be seen in these figures, and it will be interesting to notice the differences in the structures with the more complicated geometries, which will be presented in the next chapter.

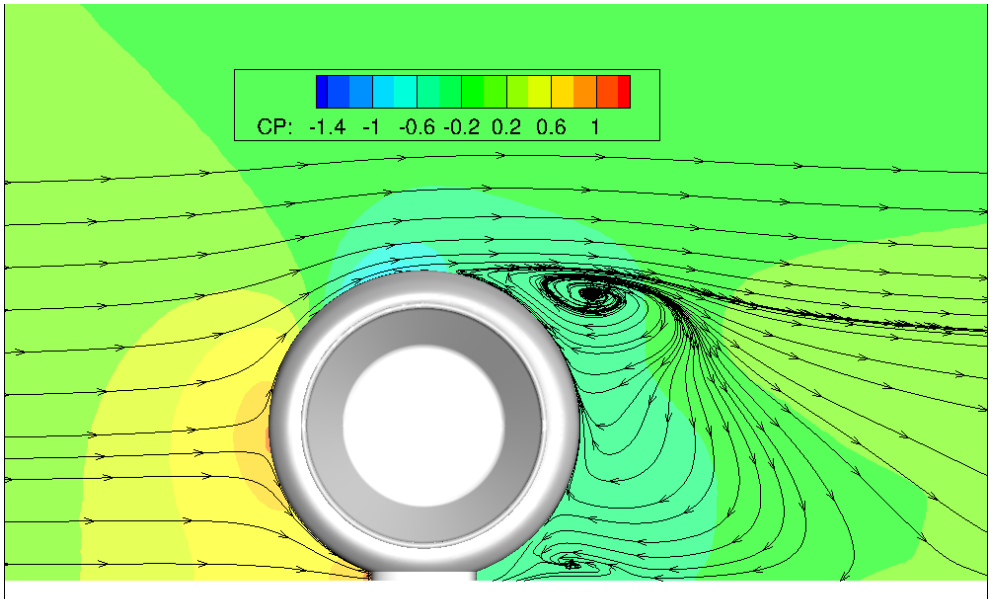

Figure 3.6: Pressure contours and streamlines on the centreline

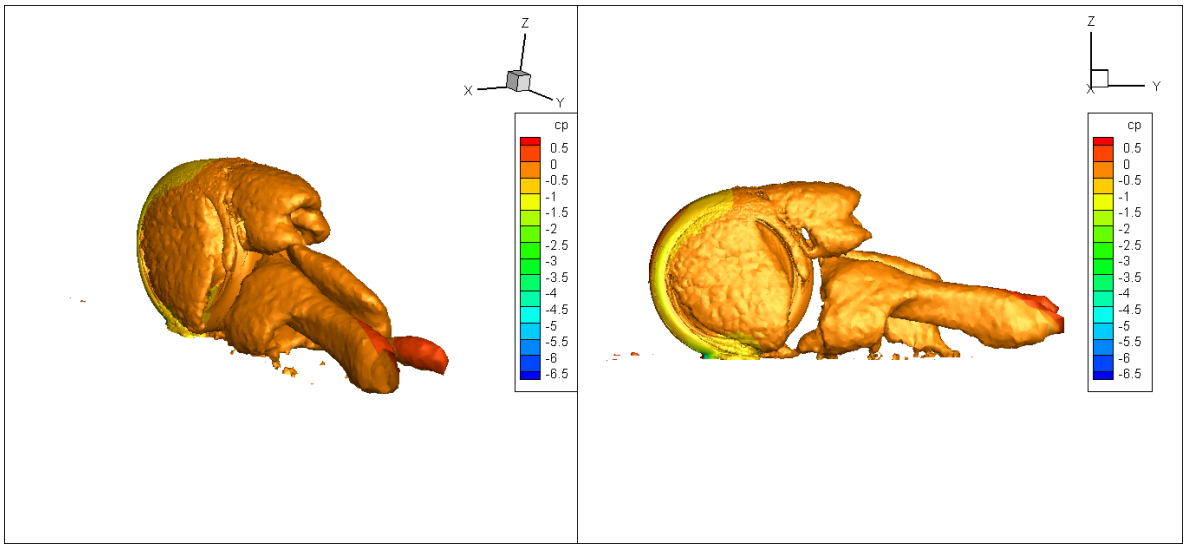

Figure 3.7: Qcriterion

Chapter 4

Results and Discussion

In the previous chapter, the baseline case with the geometry investigated by Fackrell was used in order to validate the initial results and determine the parameters that were used for the rest of the simulations. The more complicated cases will be presented in this chapter in the form of comparisons of different characteristics. The body forces and their coefficients will be examined initially along with the pressure distribution around the wheel. Subsequently, the different flow features due to the change in models will be analysed and a comparison of the computational costs of these simulations will be presented. The discussion will be integrated into each of those sections and finally, the comparative analysis for all step heights and camber angles will be presented and discussed thoroughly.

4.1 Comparison of Different Models

The three additional geometries that were described in the second chapter were tested for the present section. Firstly, the baseline wheel with a grooved tyre was studied, while a Grid Convergence Study was also performed for this geometry. Then, the flow field around the wheel with a realistic rim was examined in order to identify the flow structures

caused by differences in the rim area. Finally, a combination of both was created in order to have more realistic results overall, since this geometry resembled an actual wheel-rim-tyre system most accurately.

4.1.1 Body Forces Coefficients

In this section, the lift and drag coefficients for all cases will be presented and discussed, as well as a Grid Convergence Study that was performed for the grooved tyre. Initially, the effects of different wheel configurations on the body forces are presented in Table 4.1. It also includes the results of the simulations that were performed for the different techniques for modelling rotation: the rotating boundary conditions (RBC) on the surface and the sliding mesh. Errors are not calculated for these cases, since no experimental data exist for the specific geometries. However, overall conclusions can be drawn from previous studies and be compared with the general tendencies of these results.

Cases	Rotation Method	C_D	ΔC_D	C_L	ΔC_L
Baseline	RBC	0.4749	–	0.2624	–
	Sliding	0.5034	–	0.27	–
Grooved tyre	RBC	0.4829	$+1.68\%$	0.233	-11.2%
	Sliding	0.498	-1.07%	0.269	-0.37%
Wheel with rim	RBC	0.4502	-5.2%	0.2103	-19.86%
	Sliding	0.438	-12.92%	0.188	-30.37%
Grooved tyre and rim	RBC	0.4565	-3.87%	0.2055	-21.68%
	Sliding	0.447	-11.2%	0.178	-34.07%

Table 4.1: C_D and C_L for all models

The drag coefficient of the grooved tyre is very close to the baseline geometry, while the lift is slightly reduced. Generally, the effect is not strong and the aerodynamic behaviour is not significantly altered. On the other hand, the addition of a realistic rim to the initial geometry affects the forces that act on the wheel greatly. Both coefficients are

reduced significantly, especially with the use of the sliding mesh. The more complex configuration is influenced by the two alterations in geometry, since the drag is lower, but not as much as the simple rim case would suggest, while the lift coefficient is decreased even further. Overall, the lift force is much more sensitive to the changes in geometry, while the drag is affected but not as intensely.

In order to verify that the results of the above simulation were also in the range of convergence, a grid convergence study was performed also for the grooved wheel. The methodology that was followed was described in the previous chapter and the outcomes will be presented below. Tables 4.2, 4.3 and 4.4 present the data needed for the calculation of the GCI and the variables that were computed in the process.

#	Mesh	Elements
1	fine	$6.2 \cdot 10^6$
2	medium	$4.5 \cdot 10^6$
3	coarse	$3.6 \cdot 10^6$

Table 4.2: Grooved wheel grid levels

		C_D	C_L
1	fine	0.4891	0.252
2	medium	0.4829	0.2468
3	coarse	0.4698	0.233

Table 4.3: C_D and C_L for different mesh levels

	γ	ε_{12}	ε_{23}	GCI_{12}	GCI_{23}	$\mathscr{R}$
C_D	1.84	0.013	0.027	0.03	0.064	1.012
C_L	2.41	0.021	0.056	0.04	0.112	1.054

Table 4.4: Grid converge index analysis

The values for both coefficients converge with the refinement of the grid. This is obvious by looking at the initial coefficients and is reinforced by the calculation of the variables. The results show that the computed values are in the asymptotic range. Therefore, since the fine mesh would be too computationally expensive, the medium mesh was used for all simulations thereon. It is important to note that the differences between the values are slightly larger than the ones for the baseline case, proving that more complicated geometries become more grid dependent. Thus, if great accuracy is required, a larger number of elements will also be necessary, but relatively good results can be also acquired by a coarser mesh.

4.1.2 Pressure Distribution and Separation

The pressure coefficient around the centreline of the wheel will be compared between all models in order to identify the differences in the flow field. It is important to note that for the two grooved models the midplane coincides with the centre of the middle groove. Therefore, the pressure is expected to be different, since the flow field in significantly more unstable in the grooves.

In Figure 4.1 the differences of C_P among the models can be seen. The baseline model reaches a lower pressure coefficient than the rest, at the separation area. This can also justify the movement of the separation point slightly rearward for all the models compared to the Fackrell case. It can also be noticed that the wheel with the combination of both a grooved tyre and realistic rim has a significantly higher top pressure coefficient at the contact patch area. Furthermore, although the front part of the wheel has the same pressure distribution, at the rear part it can vary greatly, since the flow there is unsteady and can be altered easily by different geometrical features.

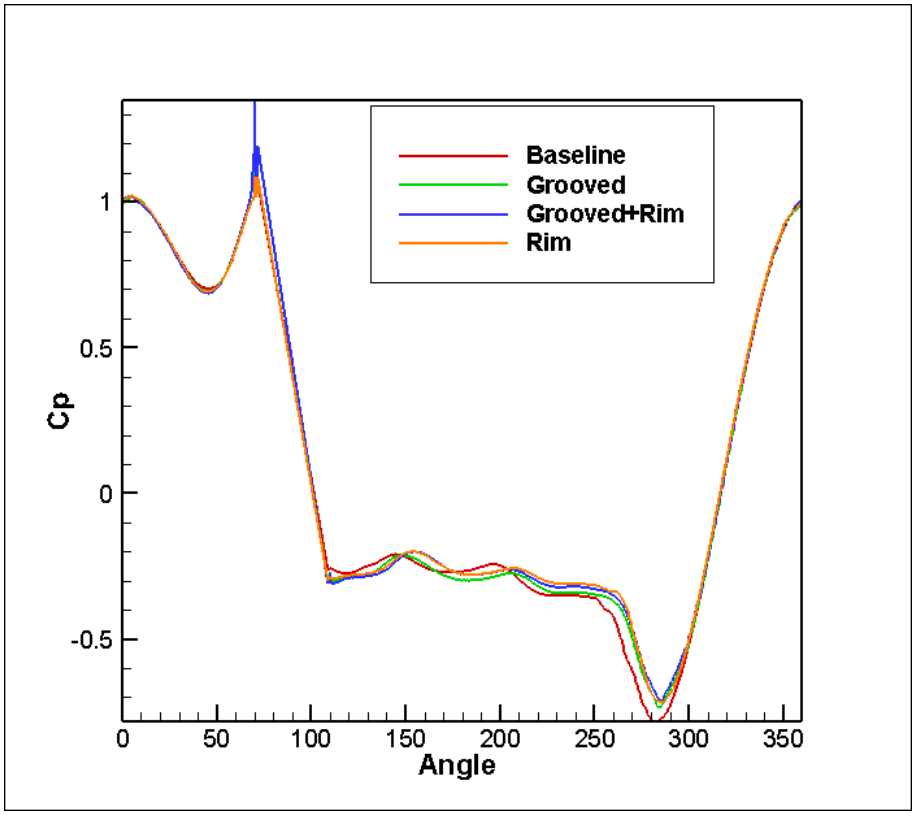

Figure 4.1: Pressure distribution on the centreline of the wheel for all cases

Additionally, the C_P contours along with streamlines on the central plane of the domain can be seen in Figure 4.2. The rim affects the pressure distribution around the wheel much more than the grooves. It can be noticed that the existence of grooves on the tyre causes the separation to occur slightly rearwards compared to the baseline case, but the change is minimal. On the other hand, the flow field caused by the wheel with the rim is transformed at the wake area compared to the previous ones. The low pressure region is shrunk, while the vortex at the bottom is enlarged. This could occur due to the vortical structures in the rim region which connect with the contact patch and the near wake. Consequently, the pressure distribution is influenced mostly by alterations at the rim area rather than the slight differences in the tyre geometry.

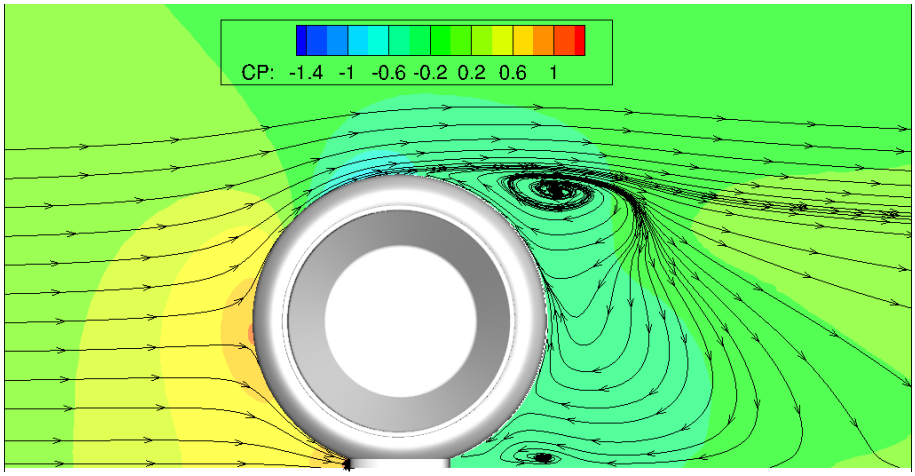

(a) Grooved

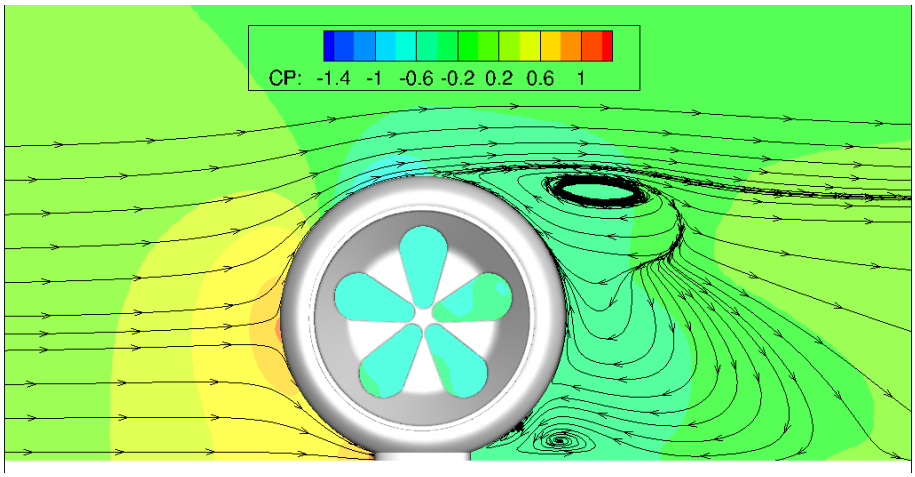

(b) Wheel with rim

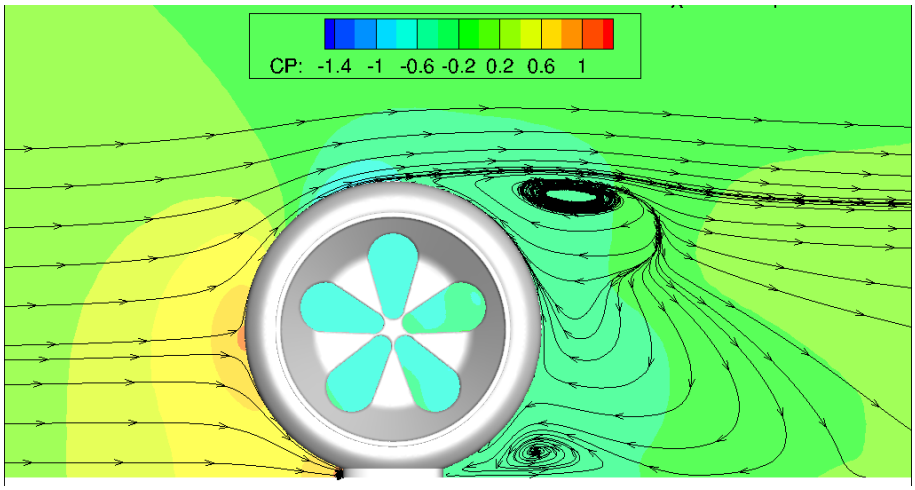

(c) Grooved with rim

Figure 4.2: C_P contours and streamlines on the centreline

4.1.3 Flow Field

In this section, the specific flow structures that form around the wheel for each different model will be described and discussed. Previously the vortices at the wake and the rim area were mentioned for the baseline case. The differences when integrating a more complicated geometry will be more visible on the flow field. Figure 4.3 presents isosurfaces of Q criterion equal to 2500 and 35000 respectively. Thus, different flow structures can be isolated and identified. When considering the lower values of Qcriterion, bigger and more robust structures can be observed, but for larger values, smaller details can be recognised. This can be useful in order to separate the vortices that occur in the wake region and the intense turbulence in the rim area.

The first two figures show the flow structures around the grooved wheel. Initially, it is very similar to the baseline case. The counter rotating vortices at the wake, are as strong but the grooves cause the separation area at the top to almost split into an upper and lower region, altering its geometry. This occurs because of the grooves, where, as can be seen in Figure 4.9b, small vortices are generated. When reaching the separation region, these connect and feed into the larger vortical area rearward. The incorporation of the rim to the baseline geometry, affects the flow field differently. The counter rotating vortices at the wake are weakened, while those connected to the contact patch and the ground become more intense. The flow in the rim area is characterised by small fluctuations in several locations as seen in 4.9d. In this figure, it is also possible to identify the creation of the large wake vortex. Finally, the integration of both geometry alterations, causes a combination of both flow fields. The wake is long but not as strong as the grooved geometry, since it is affected by the flow that escapes the rim. The top vortex is closer to the grooved case, but the effect is not as eminent. Overall, the existence of a rim affects the flow field much more than the addition of grooves.

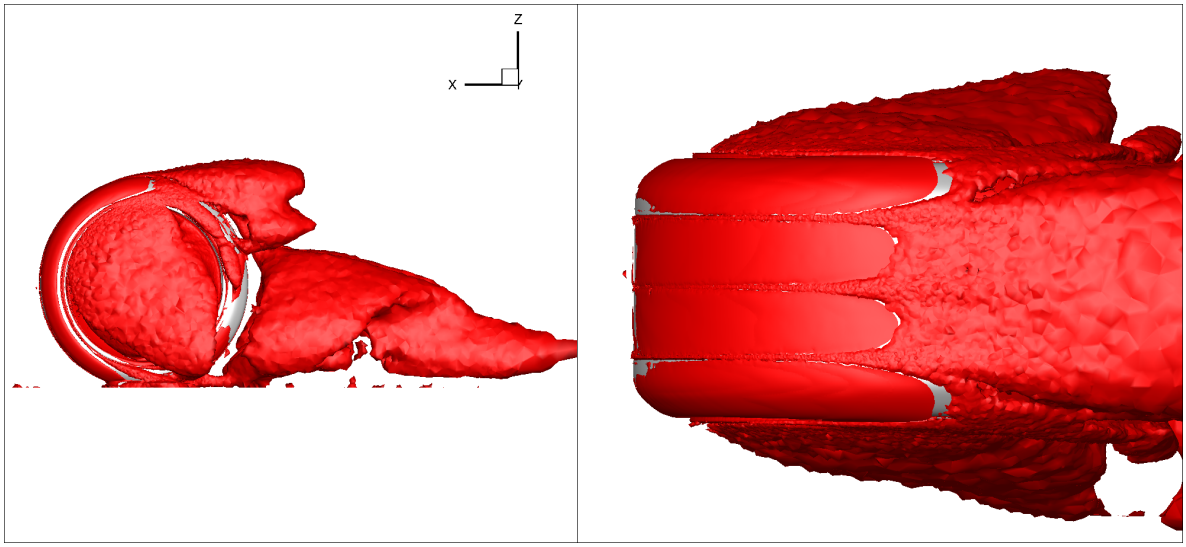

(a) Grooved, Q=2500

(b) Grooved, Q=2500

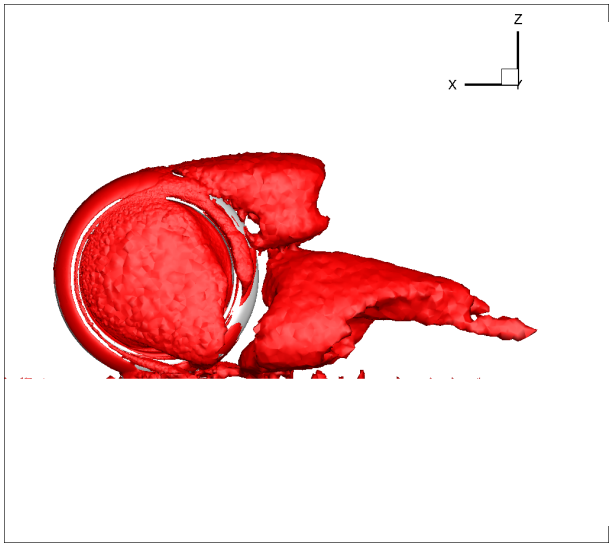

(c) Wheel with rim, Q=2500

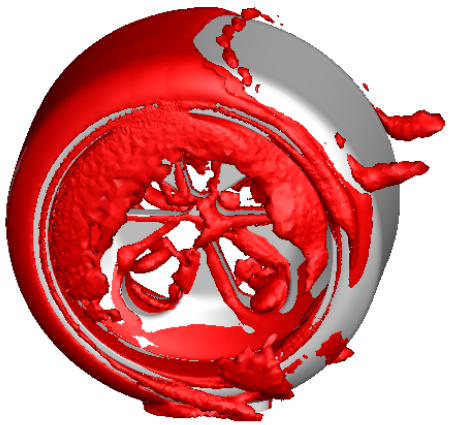

(d) Wheel with rim, Q=35000

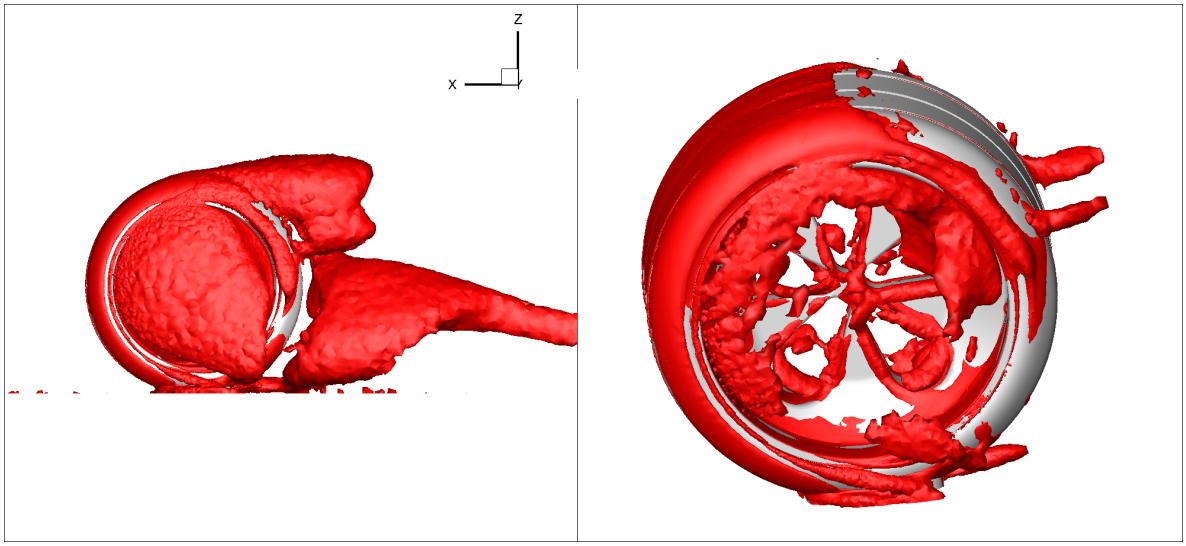

(e) Grooved with rim, Q=2500

(f) Grooved with rim, Q=35000

Figure 4.3: Qcriterion isosurfaces for the three wheel models

4.1.4 Computational Cost

In this section, the simulations that were performed will be compared based on their accuracy and their computational cost. This is especially useful to contrast the results between the sliding model and the steady state cases where RBC were used, while it is also interesting to identify the different costs for all the grid levels. The computational cost is going to be described as a function of the wall clock time needed for the shortest simulation which was the coarse mesh for the baseline geometry.

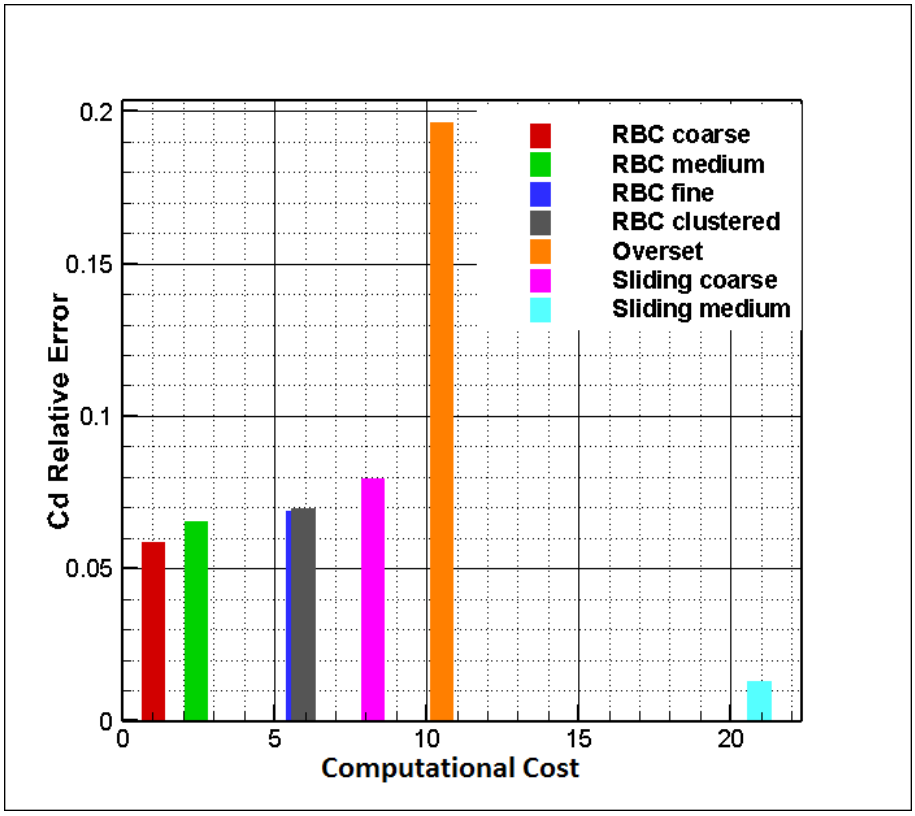

Figure 4.4: Computational cost of the baseline case

Figure 4.4 shows the relative error of C_D for all the grids and methods that were used for the baseline case. The overset mesh is by far the worst option for this problem, since it produces great error, while demanding a lot of time for the simulations. The steady state simulations with RBC require the least time but also have significant error. However, this

is not altered greatly by the refinement of the grid. The most accurate method was the sliding mesh, but only the medium mesh produced this outcome. The coarse, although being much more computationally expensive than the steady state simulations, was also much less accurate.

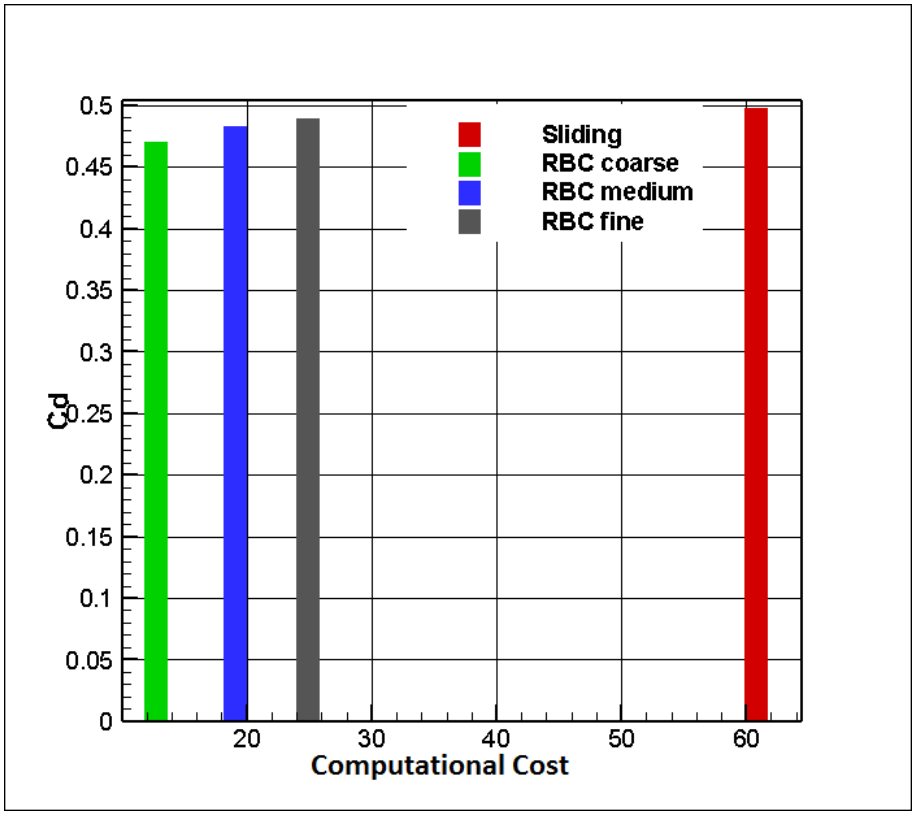

Figure 4.5: Computational cost of the grooved wheel

In Figure 4.5 the drag coefficients are shown compared to the computational cost for each simulation. There is no exact experimental data for the grooved wheel case, so the results are being analysed. Again, the sliding mesh is much more expensive, however it can be assumed that it also is more accurate. Overall, it can be concluded that the steady state simulations produce reasonable results for all grid levels, but if particular accuracy is required, then a reasonable sliding mesh will provide it.

4.1.5 Forces Distribution

In this section, the distribution of drag and lift on the different regions of the wheel is going to presented and discussed. This distribution is especially important in automotive applications when considering the effect of the upper and lower parts of the wheel. The lower part influences the flow more significantly, since the upper region is usually covered by a wheelhouse cavity. The distribution between rim and tyre is also included, but this might not demonstrate the actual effect these parts have on the aerodynamic behaviour of a wheel, since the forces relate significantly to the frontal area, which is mostly occupied by the tyre. The data in Tables 4.5 and 4.6 is presented by showing the percentage of each region to the overall force. The regions are split according to their location and type, where U and L represent upper and lower respectively, and T and R represent tyre and rim. The exact division of surfaces is depicted in Figure 4.6.

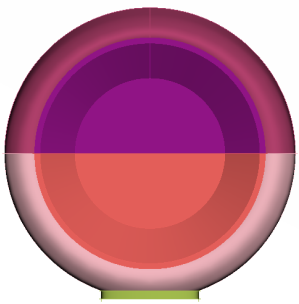

Figure 4.6: Division of the wheel into regions

The drag is divided in the upper and lower part almost equally, but the upper part has a slightly greater effect on it. This could influence wheel modelling negatively, since the aerodynamic characteristics of an isolated wheel might differ more from those of a wheel in a full vehicle. It is also important to note that, although the rim seems to not affect the flow as much, the incorporation of a different rim geometry influences the drag greatly.

DRAG %	UT	UR	Upper	LT	LR	CP	Lower	Rim	Tyre
Baseline	35.65	21.30	56.95	52.91	-8.52	-1.35	43.05	12.78	87.22
Grooves	36.02	22.57	58.59	50.72	-8.70	-0.62	41.41	13.87	86.13
Rim	36.36	18.85	55.21	50.33	-4.21	-1.33	44.79	14.63	85.37
Grooves+Rim	36.62	18.86	55.48	49.78	-4.17	-1.10	44.52	14.69	85.31

Table 4.5: Drag distribution on the wheel

LIFT %	UT	UR	Upper	LT	LR	CP	Lower	Rim	Tyre
Baseline	148.62	-114.62	33.99	-50.20	116.21	0.00	66.01	1.58	98.42
Grooves	154.59	-112.51	42.08	-54.96	112.94	-0.05	57.92	0.43	99.57
Rim	165.24	-141.43	23.81	-64.76	140.95	0.00	76.19	-0.48	100.48
Grooves+Rim	167.25	-144.05	23.20	-67.19	144.05	-0.06	76.80	-0.06	100.06

Table 4.6: Lift distribution on the wheel

The lift behaves differently for all parts of the wheel. The lower region causes the largest percentage of lift, which is actually further increased by the addition of a realistic rim geometry. Many regions produce downforce, which would be significant in the case of a full car, but they are mostly cancelled out the very high lift values at other regions. The tyre is completely responsible for the generation of lift, specifically the upper part, which has a very high value for all cases.

The forces that affect the step of the contact patch are also important, since it seems to affect the flow differently than a realistic contact patch area. The drag is negative, although lower part of the tyre has a big contribution to the overall drag. However, regarding the lift, the effect of the contact patch area is even smaller and does not influence the flow at all. It is interesting, though, that the lift at that area is affected more by the addition of grooves than the realistic rim geometry.

4.2 Step Height Sensitivity Study

Seven different step heights were tested for this section, as was described in the second chapter. The results will be presented as a form of C_D and C_L comparison and C_P contours on the ground plane to identify the differences at the contact patch region. In Figure 4.7 the forces coefficients are presented for the different step heights that were tested. The results for both rotation modelling techniques (Rotating Boundary Condition (RBC) and Sliding mesh) are shown for comparison.

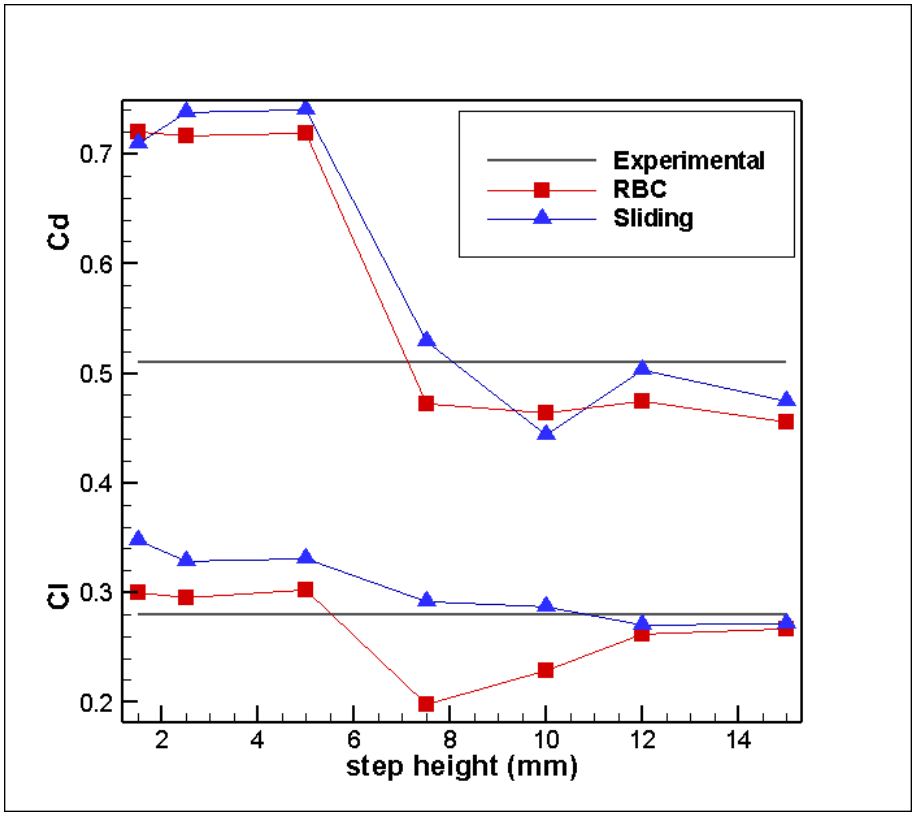

Figure 4.7: Drag and Lift coefficients for the step heights

The results were not those expected considering the outcomes of previous studies. Diasinos et al. [1] noticed that, by reducing the height of the contact patch, the coefficients converged to the correct value, very close to the experimental. It was concluded that, by increasing the step height, the strength of the primary wheel vortices is reduced along

with the central downwash, causing the separation point to shift forward. Simultaneously, the total drag on the wheel is also reduced. It is important to note that in the study by Diasinos et al. a y^+ equal to 1 was used, allowing for significantly smaller step sizes with the good quality mesh. Thus, while the small step sizes used in that study, produced highly accurate results, the larger heights caused the value of drag to drop significantly.

A similar effect can be noticed in Figure 4.7, where the C_D drops for higher height values. However, a significant rise occurred for lower heights, which dropped the accuracy greatly. Specifically, while the values were around the same level for a range between 7.5*mm* and 15*mm* with variable accuracy levels, the heights from 1.5*mm* to 5*mm* caused an extreme increase in drag coefficient and consequently error. The effects were similar for both rotation modelling methods, with small discrepancies for specific heights.

The above differences were not as visible for the lift coefficient, which has been found to not be very sensitive to the height of the contact patch, since the phenomena that occur there do not influence it directly. However, the error for lower values was still increased compared to the initial results.

It is important to note that for the present project a Y^+ equal to 30 was used, and thus the effect on the contact patch modelling might be more intense. Although the good quality of the mesh was ensured even for the cases with the smallest height, the number of elements between the wheel and the ground might not me enough to produce accurate results. Some flow features might also be concerned with the effect of very high drag, therefore it is important to observe the flow on the ground around the contact patch. These can be seen in Figure 4.8.

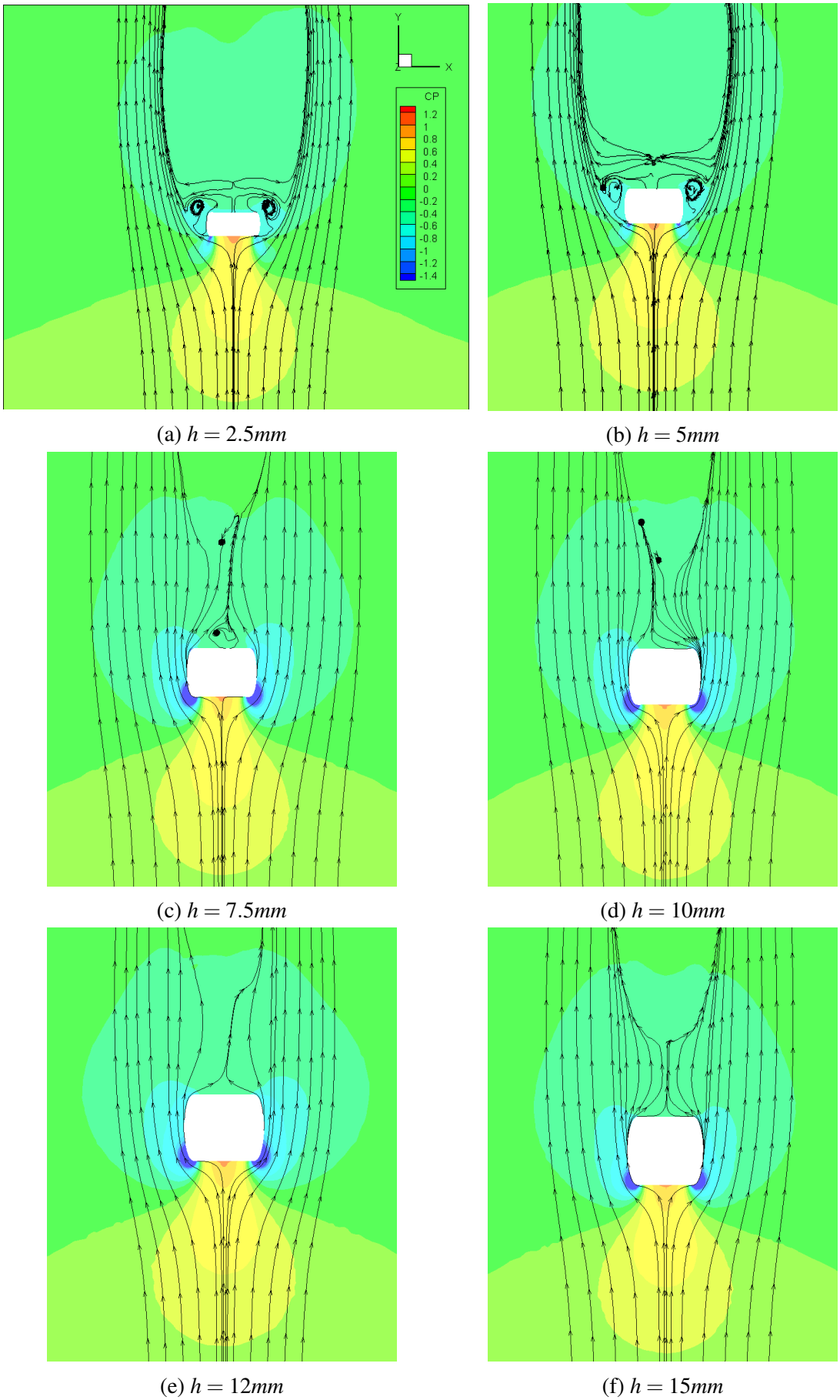

(a) $h = 2.5mm$ (b) $h = 5mm$

(c) $h = 7.5mm$ (d) $h = 10mm$

(e) $h = 12mm$ (f) $h = 15mm$

Figure 4.8: C_P contours and streamlines on the ground plane

It can be observed that, for bigger contact patches, the flow remains attached at the ground plane. The areas of very low pressure at the sides are larger, while the separation region at the wake is located much farther back. As the height, and consequently the size, of the step size is reduced, the flow behind the wheel becomes more complex, creating turbulent regions in the near wake. Especially for the smallest values two counter rotating vortices are created at the rearward sides. These affect the flow field significantly by generating a large separation area behind the wheel. This, may be the reason for the great increase in drag that occurs with lower step sizes.

It can be hypothesized that the dimension that plays the most important role is not the height but the width of the contact patch in the longitudinal direction. The smallest the width, the larger the separation area behind the wheel which causes the increase in drag. It can be said that a very small contact patch area is not realistic, since in actual automotive applications a loaded tyre will result in a larger contact area. Thus, although the height might affect the reduction of drag, the width has a bigger impact on the overall flow field of the wheel, increasing the recirculation regions behind the contact patch. Consequently, the final drag coefficient is much higher than it should be for a more realistic geometry.

The lift force is not significantly affected by these newly created vortices, since the pressure at the ground level is low for all cases and does not change greatly for the different geometries. However, there seems to be a slight correlation between the altered step geometry and the lift coefficient. When the separation point is moved forward, the peak low pressure is reduced, causing the further reduction of lift. Also in this case, a more realistic wheel model, with proper loading would provide a better contact area, and the results would converge to a more accurate value. Overall, the study of the contact patch region is a very complicated topic that needs further investigation regarding all the parameters that affect it.

4.3 Camber Angle Sensitivity Study

A wheel's camber angle can be very influential for a vehicle's stability and is usually not considered an aerodynamic characteristic of the vehicle itself, since its existence is usually dictated by a more important need concerning the overall behaviour [40]. However, on an isolated wheel the camber angle can significantly affect the flow field around it, thus altering the flow that reaches other components. In this section, the drag and lift coefficients for three different camber angles will be presented and discussed, while the vortical structures that occur due to change in tilt angle are going to be identified. Table 4.7 presents the forces coefficients and the changes that occur because of the camber angle for each case.

Cases	Rotation Method	C_D	ΔC_D	C_L	ΔC_L
Baseline	Sliding	0.4749	–	0.2624	–
	RBC	0.5034	–	0.27	–
1^o camber	Sliding	0.6041	+18.45%	0.2912	+4%
	RBC	0.5972	+17.1%	0.2854	+1.93%
2^o camber	Sliding	0.6127	+20.14%	0.2984	+6.57%
	RBC	0.5813	+13.98%	0.2935	+4.82%
3^o camber	Sliding	0.6235	+22.25%	0.3083	+10.11%
	RBC	0.5998	+17.61%	0.2986	+6.64%

Table 4.7: C_D and C_L for all camber angles

It is important to note that the forces of the steady state simulations with Rotating boundary conditions on the surface of the wheel had strong oscillations, showing the severe unsteadiness of the cases. Therefore, the results of the sliding mesh will be considered more trustworthy, but the steady state ones will be taken into account as well. It can be observed that both coefficients increase with the application of a higher camber angle. The effect is considerable for the C_D which is very high, proving that the flow is altered greatly by the inclination of the wheel. The influence of the increased angle is obvious

for both rotating methods, although the values have a steady deviation among them. It can be deducted that strong vortical structures are created around the wheel affecting the whole flow field. Therefore, Q criterion isosurfaces were created to isolate the differences between the baseline case and the addition of camber angles.

In Figure 4.9 the isosurfaces of $Q = 2500$ show a completely non symmetric flow field. At the lower part of the wheel, strong vortical structures occur at the side towards which the wheel is tilted. However, these fade at the near wake, while the vortices at the opposite side are significant for much longer and it also extends much wider. The most important feature of the flow field is a new vortex that appears at the top outer side of the wheel. It creates a side separation area that increases the drag, but is it distinct from the normal separation region that occurs in the baseline case. Some of these effects slightly fade as the camber angle increases, since for the smaller angle the flow field is much more complicated around the wheel.

Overall, the camber angle affects the flow greatly and should be studied further. Since for some applications wheel inclination is essential, it can be vital to study the influence that it has on the flow field of other parts of the vehicle, especially on the underbody, since it has a great impact on the total drag.

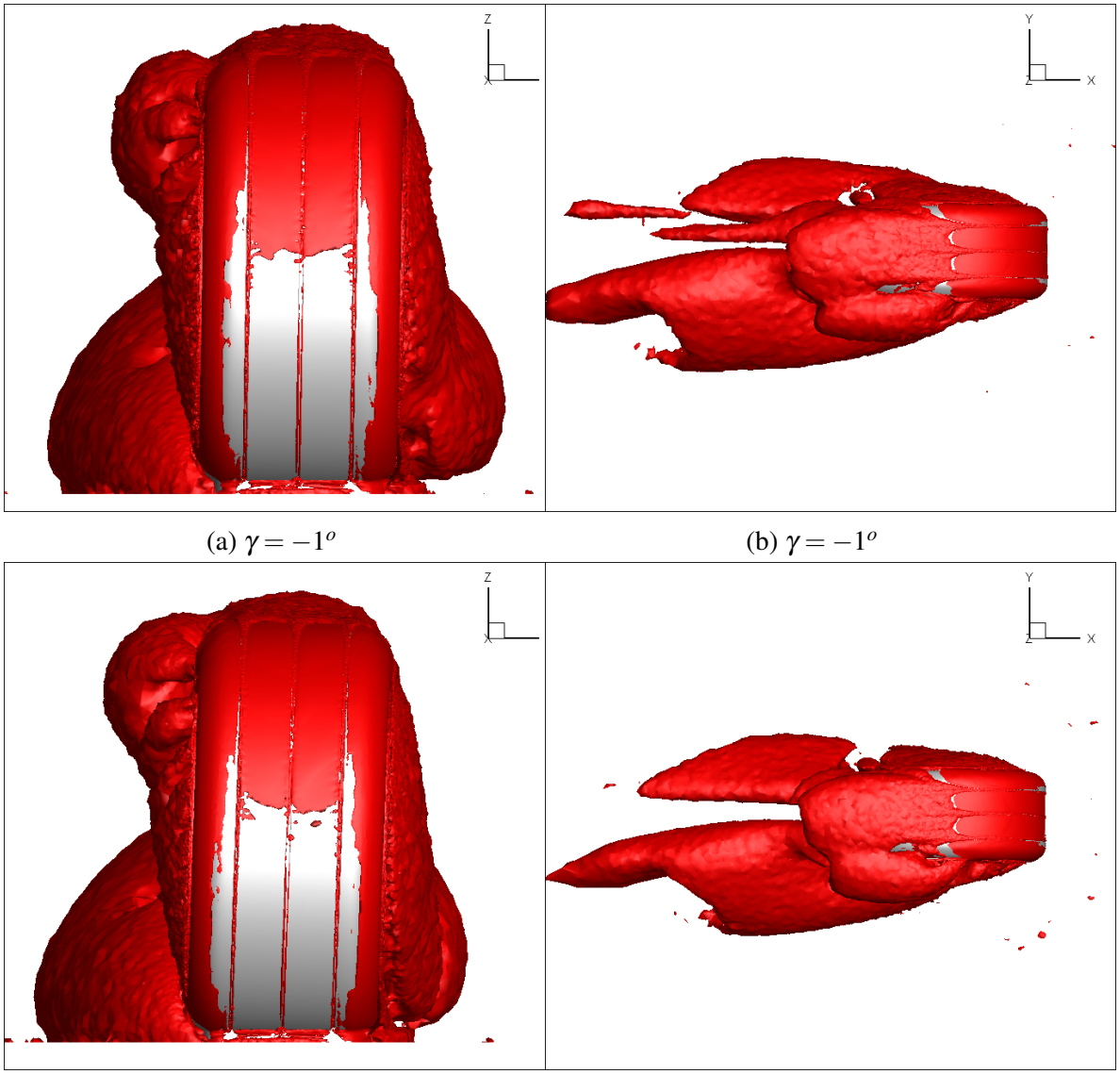

(a) $\gamma = -1^o$ (b) $\gamma = -1^o$

(c) $\gamma = -2^o$ (d) $\gamma = -2^o$

Figure 4.9: Isosurfaces of Q criterion for different camber angles

Chapter 5

Conclusions and Future Work

The present project aimed at investigating and assessing the effect of rotation modelling techniques on the case of an isolated wheel, while studying the flow field around different configurations of wheel rim tyre systems, with the use of CFD. The software ANSYS Fluent has been utilised for the duration of the thesis and both steady state and transient simulations have been performed for a Reynolds number of $530,000$.

Initially, a baseline geometry was investigated by comparing experimental data with CFD results. Three grid levels, generated by ANSA software by BETA CAE, between $5 \cdot 10^5$ and $20 \cdot 10^5$ cells, were used in order to perform a *Grid Convergence Study* by applying simple Rotating Boundary Condition on the wheel surface. The results converged to a value with a relevant error of approximately 6.8% for the drag and 6.2% for the lift compared to the experimental. When the same geometry was investigated using the Sliding mesh method, the errors were reduced to 1.2% and 3.5% respectively. The overset mesh method was also applied for the first time in such a geometry by creating a model, where the wheel was located $5mm$ above the ground level. This method produced less accurate results, since the problem solved was not the exact same as the baseline case. In general, the sliding mesh proved to be the most accurate rotation modelling method for

a moderately sized grid. However, the RBC model performed reasonably well, and was significantly less computationally expensive. Therefore, the RBC model is considered an acceptable choice unless very accurate results are required.

Subsequently, three models were created in order to investigate the effect of different geometrical features on the flow field. Therefore, grooves were added to the baseline geometry and a realistic rim was also created, and these features were used separately and together to generate the three models. The comparison between the four different cases showed that the grooves only slightly affect the resulting flow field, by creating some small vortices at the top separation area, but the existence of a rim significantly affects the flow by altering the wake area, thus reducing the drag and the lift drastically. The combined geometry showed characteristics of both cases, with a further reduction of lift but a moderate increase of drag. Overall, the rim geometry has a greater effect on the flow, by complicating the phenomena that occur in that region. The forces distribution on different parts of the wheel was studied, since it can be important for automotive applications to isolate the values of forces to each region. The upper part affected the drag more, but this influence was reduced by introducing new geometrical characteristics to the wheel. The lift distribution was more complicated, since depending on the region there were very high positive and negative values. Generally, The lower part affected the lift force more and this became even more intense with the incorporation of grooves and rims.

The proper size of the step used at the contact patch area to generate good quality grids was also investigated. Seven different sizes were tested, ranging from 0.36% to 3.6% of the wheel's diameter. The results showed that, for smaller values of step height, vortices are created right behind the wheel, possibly because of the small longitudinal width of the step. On the other hand, when a greater height is used, the drag drops because the separation point is moved rearward. Consequently, unless a realistic loaded

tyre geometry is used, it is considered that a higher step of around 2.4% of the wheel's diameter will produce more accurate results.

The influence of the camber angle on the flow field around the wheel was examined, since it can be very important for other parts of a vehicle. Three different values of camber were tested, -1^o, -2^o and -3^o,and the results were similar for all three. The drag increases significantly, since the flow becomes asymmetric, the vortices are exaggerated and new ones are created on the opposite side of the camber. The lift was not affected as much, but it was clear that is also has a tendency to rise. Further research is required in this area to investigate the effects of this flow on other parts of a vehicle.

Generally, the isolated wheel case has been thoroughly studied, but some issues are still unresolved. The modelling of rotation and the connection to the groundplane have yet to be settled. The overset mesh technique is a very interesting method that could resolve both of those problems. Thus, if the limitations set by the existing software were to be overcome, the overset method should definitely be incorporated and tested more. Until that occurs, the step at the contact patch might be unavoidable for not loaded tyres. Therefore, the minimisation of its effects on the flow field around that area should be researched further, for different grid types and wheel geometries. Subsequently, introducing wheels with a camber angle to full vehicle CFD models, would contribute to a more accurate view on their aerodynamic behaviour. Finally, establishing a standardised wheel model for experimental and CFD application, would provide great benefits in terms of being able to compare different modelling techniques and incorporation of new details.

Appendix A

Meshes

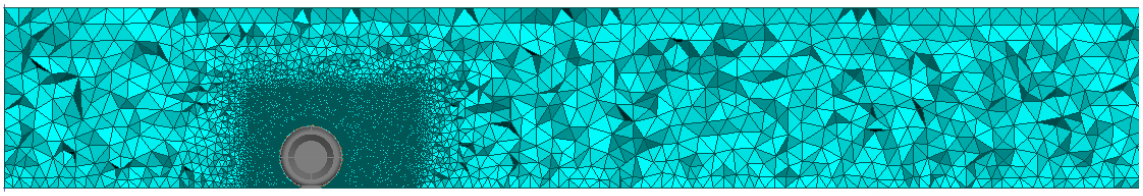

Figure A.1: Baseline clustered box

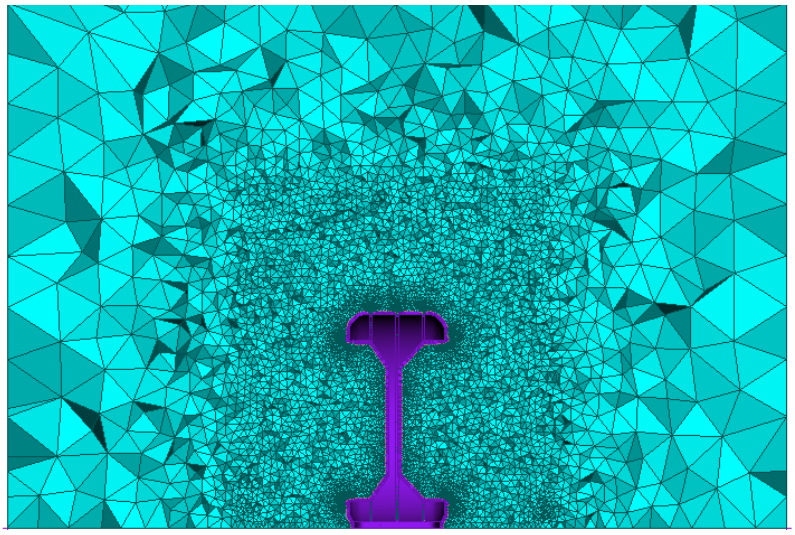

Figure A.2: Frontal view - grooved wheel

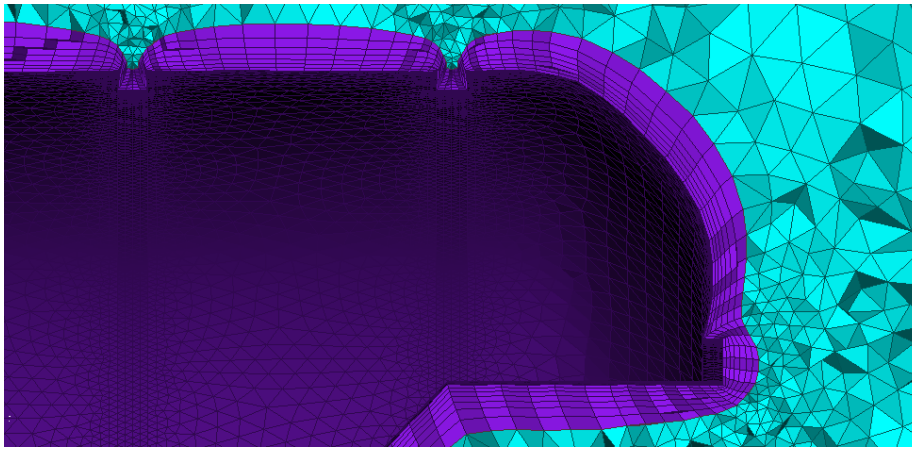

Figure A.3: Detailed view - grooved wheel

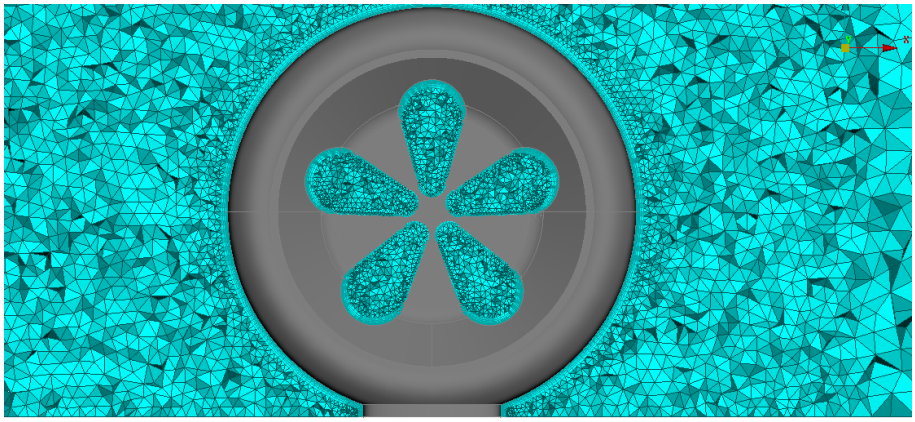

Figure A.4: Side view - wheel with rim

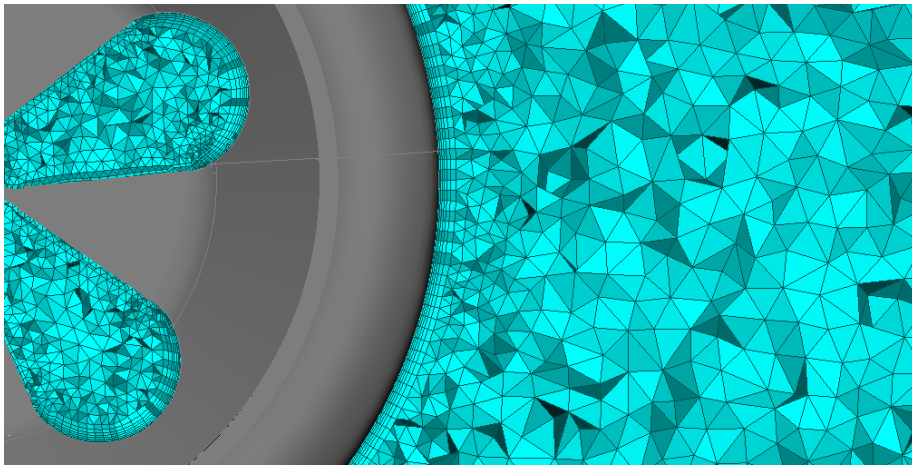

Figure A.5: Detailed view - wheel with rim

Appendix B

C_L and C_D over time for unsteady simulations

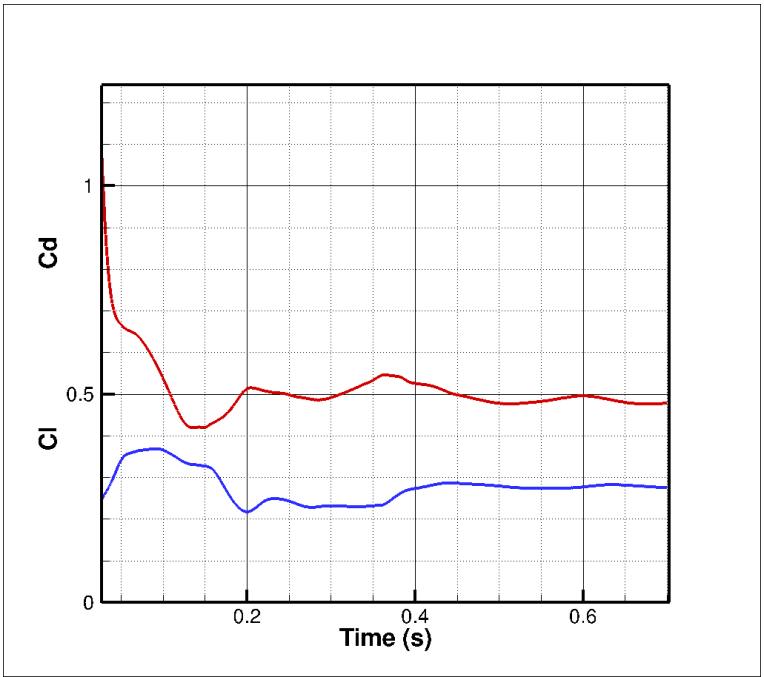

Figure B.1: C_L and C_D over time for the grooved wheel

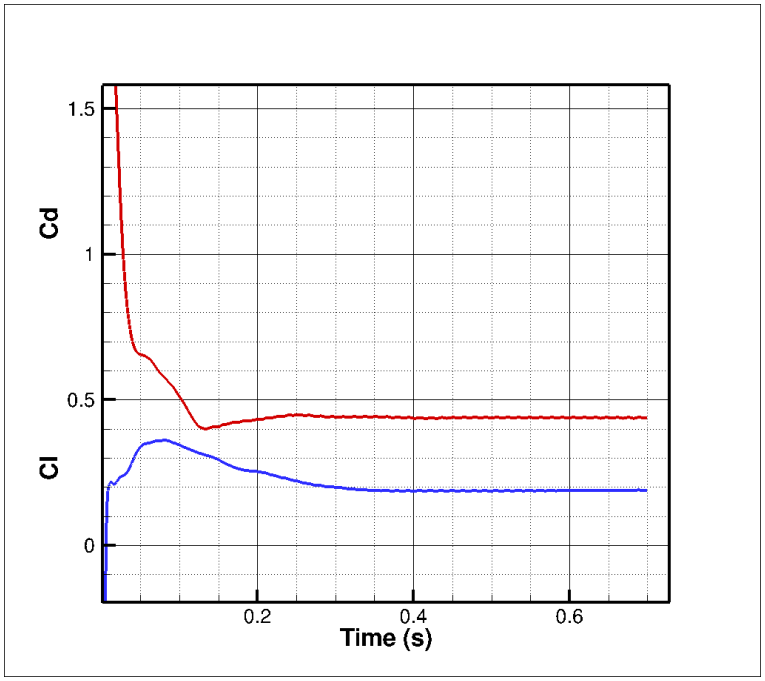

Figure B.2: C_L and C_D over time for the wheel with a rim

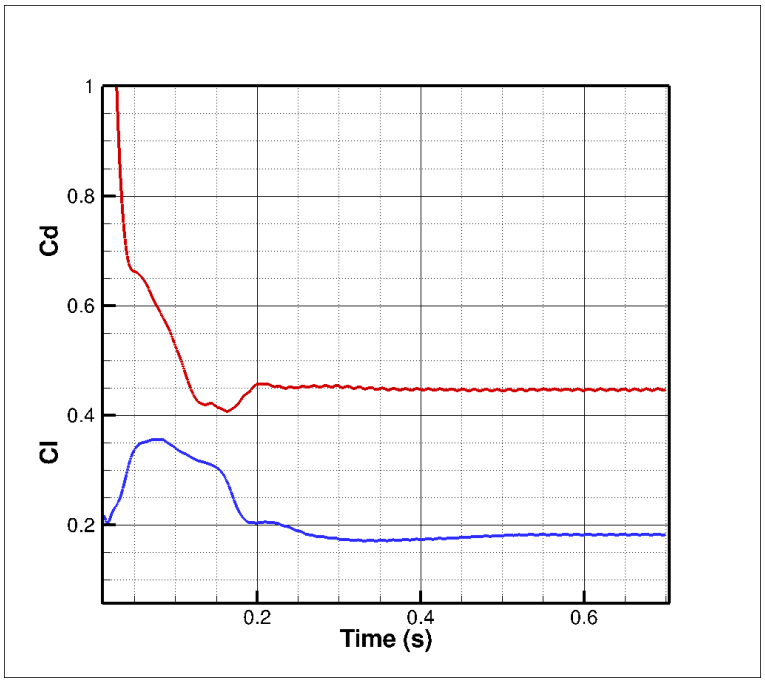

Figure B.3: C_L and C_D over time for the grooved wheel with a rim

Appendix C

Matlab Codes

C.1 C_P transformation from Cartesian to Polar coordinates

```
clear all;
clc;
close all;



file = csvread('cp.csv',1,0);
Y = file(:,1);
Z = file(:,2);
cp1 = file(:,3);


    N = length(Z);
```

```
    for i=1:N
a1(i) = atan2(Z(i) - 0.2079625, Y(i)) * 180/pi;
if (Z(i) - 0.2079625) < 0
a2(i)=1(i)+360;
else
a2(i)=a1(i);
end
a3(i)=a2(i)-180;
if a3(i)¡0
a3(i)=a3(i)+360;
end
end


    angle=1000*ones(1,N);

for i=1:N
for j=1:N
if angle(i)¿a3(j)
angle(i)=a3(j);
id=j;
end
end
a3(id)=100000;
cp(i)=cp1(id);
end
```

angle=angle';

cp=cp';

$cp_num = [angle, cp]$;

plot(angle,cp)

C.2 Error Norms calculation

clc;

clear all;

close all;

format long;

%Load data

%experimental

cp=importdata('cp-f.txt');

%numerical

%Non-dimensionalization of the x coordinate of the numerical data

cp1(1,1)=cp(1,1);

cp1(end,1)=cp(end,1);

%Interpolation

$cp1 = interp1(cp_num(:,1), cp_num(:,2), cp(:,1));$

```
    %Compute error vectors
e=abs(cp1-cp(:,2));

    %Compute error norms

    %L0
L0=max(e);

    %L1
L1=mean(e);

    %L2
```

$L2 = sum(e.^2)/length(e);$

```
    %Collect all vector norms
M=[L0; L1; L2]
```

References

[1] Sammy Diasinos, Tracie J. Barber, and Graham Doig. The effects of simplifications on isolated wheel aerodynamics. 2015.

[2] James Mcmanus and Xin Zhang. A computational study of the flow around an isolated wheel in contact with ground. 2006.

[3] ANSYS FLUENT. 2016.

[4] J.Y. Wong. *Theory of Ground Vehicles*. Wiley-Interscience. Wiley, 2001.

[5] J. Katz. *Race Car Aerodynamics: Designing for Speed*. Robert Bentley, Incorporated, 1996.

[6] R.H. Barnard. *Road Vehicle Aerodynamic Design: An Introduction*. Mechaero Publishing, 2009.

[7] Wolf-Heinrich Hucho. Chapter 4 - aerodynamic drag of passenger cars. In Wolf-Heinrich Hucho, editor, *Aerodynamics of Road Vehicles*, pages 106 – 213. Butterworth-Heinemann, 1987.

[8] Alexander Wäschle. The influence of rotating wheels on vehicle aerodynamics - numerical and experimental investigations. *SAE Technical Paper*, 2007.

[9] Todd H. Lounsberry, Mark E. Gleason, Satheesh Kandasamy, Khaled Sbeih, Richa Mann, and Bradley D. Duncan. The effects of detailed tire geometry on automobile aerodynamics - a cfd correlation study in static conditions. *SAE Int. J. Passeng. Cars-Mech. Syst.*, 2:849–860, 2009.

[10] Satheesh Kandasamy, Bradley Duncan, Holger Gau, Fabien Maroy, Alain Belanger, Norbert Gruen, and Sebastian Schäufele. Aerodynamic performance assessment of bmw validation models using computational fluid dynamics. *SAE Internationa*, 2012.

[11] Sofie Koitrand and Sven Rehnberg. A computational investigation of wheel and underbody flow interaction. Master's thesis, 2013.

[12] Nicholas Simmonds, John Pitman, Panagiotis Tsoutsanis, Karl Jenkins, Adrian Gaylard, and Wilko Jansen. Complete body aerodynamic study of three vehicles. *SAE International*, 2017.

[13] Lee Axon, Kevin Garry, and Jeff Howell. The influence of ground condition on the flow around a wheel located within a wheelhouse cavity. 1999.

[14] A. F. Skea, P. R. Bullen, and J. Qiao. Cfd simulations and experimental measurements of the flow over a rotating wheel in a wheel arch. 2000.

[15] Krajnovic S, Sarmast S, and Basara. Les of the flow around a generic wheel in a wheelhouse. *ASME 2010 3rd Joint US-European Fluids Engineering Summer Meeting: Volume 1, Symposia-Parts A, B, and C ():2681-2692*, 2010.

[16] Sinisa Krajnovic. Exploration and improvement of road vehicle aerodynamics using les. 2011.

[17] John Edward Fackrell. The aerodynamics of an isolated wheel rotating in contact with the ground. 1974.

[18] Lee Axon, Kevin Garry, and Jeff Howell. An evaluation of cfd for modelling the flow around stationary and rotating isolated wheels. In *SAE Technical Paper*. SAE International, 02 1998.

[19] Alexander Wäschle, Stephane Cyr, Timo Kuthada, and Jochen Wiedemann. Flow around an isolated wheel - experimental and numerical comparison of two cfd codes. In *SAE Technical Paper*. SAE International, 03 2004.

[20] P.R.K. Dassanayake, D. Ramachandran, L. Salati, T.J. Barber, and G.C. Doig. Unsteady computational simulation of the flow structure of an isolated wheel in contact with the ground. *School of Mechanical and Manufacturing Engineering, University of New South Wales, Sydney, NSW*.

[21] P Lesniewicz, M Kulak, and M Karczewski. Aerodynamic analysis of an isolated vehicle wheel. *Journal of Physics: Conference Series*, 530(1):012064, 2014.

[22] P Lesniewicz, M Kulak, and M Karczewski. Vehicle wheel drag coefficient in relation to travelling velocity - cfd analysis. *Journal of Physics: Conference Series*, 760(1):012014, 2016.

[23] Axerio-Cilies J, Issakhanian E, Jimenez J, and Iaccarino G. An aerodynamic investigation of an isolated stationary formula 1 wheel assembly. *ASME. J. Fluids Eng.*, 2(134), 2012.

[24] A. J. Sprot, D. B. Sims-Williams, and R. G. Dominy. The aerodynamic characteristics of a fully deformable formula one wind tunnel tyre. *SAE Int. J. Passeng. Cars - Mech. Syst.*, 5:1026–1041, 04 2012.

[25] Stefano Spagnolo, Xin Zhang, Zhiwei Hu, Oksana Stalnov, and David Angland. Unsteady aerodynamics of single and tandem wheels. *Journal of Fluids and Structures*, 69:121 – 136, 2017.

[26] Felix Wittmeier, Timo Kuthada, Nils Widdecke, and Jochen Wiedemann. Model scale based process for the development of aerodynamic tire characteristics. In *SAE Technical Paper*. SAE International, 04 2014.

[27] Christoffer Landström, Tim Walker, Lasse Christoffersen, and Lennart Löfdahl. Influences of different front and rear wheel designs on aerodynamic drag of a sedan type passenger car. In *SAE Technical Paper*. SAE International, 04 2011.

[28] Teddy Hobeika, Simone Sebben, and Christoffer Landstrom. Investigation of the influence of tyre geometry on the aerodynamics of passenger cars. *SAE Int. J. Passeng. Cars - Mech. Syst.*, 6:316–325, 04 2013.

[29] Mark E. Gleason, Bradley Duncan, Joel Walter, Arturo Guzman, and Young-Chang Cho. Comparison of computational simulation of automotive spinning wheel flow field with full width moving belt wind tunnel results. *SAE Int. J. Passeng. Cars - Mech. Syst.*, 8:275–293, 04 2015.

[30] Bastian Schnepf, Gregoe Tsch, and Thomas Indinger. Investigations on the flow around wheels using different road simulation tools. *9th Aerodynamic Conference*, 2013.

[31] Andrew D'Hooge, Robert B. Palin, S. Johnson, Bradley Duncan, and Joaquin Ivan Gargoloff. The aerodynamic development of the tesla model s - part 2: Wheel design optimization. In *SAE Technical Paper*. SAE International, 04 2012.

[32] Bastian Schnepf, Thomas Schtz, and Thomas Indinger. Further investigations on the flow around a rotating, isolated wheel with detailed tread pattern. *SAE Int. J. Passeng. Cars - Mech. Syst.*, 8:261–274, 04 2015.

[33] Prashanta Gautam and Abhilash J. Chandy. Understanding tire acoustics through computational fluid dynamics (cfd) of grooves with deforming walls. *ASME. J. Fluids Eng.*, 2015.

[34] Charlie Lew, Nath Gopalaswamy, Richard Shock, Bradley Duncan, and James Hoch. Aerodynamic simulation of a standalone rotating treaded tire. In *SAE Technical Paper*. SAE International, 03 2017.

[35] M. A. van den Berg and X. Zhang. The aerodynamic interaction between an inverted wing and a rotating wheel. *Journal of Fluids Engineering*, 131(10), 2009.

[36] P Gruber, R S Sharp, and A D Crocombe. Friction and camber influences on the static stiffness properties of a racing tyre. *Proceedings of the Institution of Mechanical Engineers, Part D: Journal of Automobile Engineering*, 222(11):1965–1976, 2008.

[37] K.A Abd El-Gawwad, D.A Crolla, A.M.A Soliman, and F.M El-Sayed. Off-road tyre modelling ii: effect of camber on tyre performance2part i of a four part series. parts iii and iv are published in the journal of terramechanics 36(2).2. *Journal of Terramechanics*, 36(1):25 – 38, 1999.

[38] P.J. Roache. Quantification of uncertainty in computational fluid dynamics. *Annual Review of Fluid Mechanics*, 29:123–160, 1997. cited By 554.

[39] J. C. R. Hunt, A. A. Wray, and P. Moin. Eddies, Stream, and Convergence Zones in Turbulent Flows. *Center For Turbulence Research*, Report CTR-S88, 1988.

[40] Hans B. Pacejka. Chapter 1 - tyre characteristics and vehicle handling and stability. In Hans B. Pacejka, editor, *Tyre and Vehicle Dynamics (Second Edition)*, pages 1 – 60. Butterworth-Heinemann, Oxford, second edition edition, 2006.